





Article

# VIS-NIR, Red-Edge and NIR-Shoulder Based Normalized Vegetation Indices Response to Co-Varying Leaf and Canopy Structural Traits in Heterogeneous Grasslands

Hafiz Ali Imran <sup>1,2,\*</sup>, Damiano Gianelle <sup>1</sup>, Duccio Rocchini <sup>3,4</sup>, Michele Dalponte <sup>1</sup>,  
M. Pilar Martín <sup>5</sup>, Karolina Sakowska <sup>6,7,8</sup>, Georg Wohlfahrt <sup>6</sup> and Loris Vescovo <sup>1</sup>

<sup>1</sup> Sustainable Ecosystems and Bioresources Department, Research and Innovation Centre, Fondazione Edmund Mach, Via E. Mach 1, 38010 San Michele all'Adige (TN), Italy; damiano.gianelle@fmach.it (D.G.); michele.dalponte@fmach.it (M.D.); loris.vescovo@fmach.it (L.V.)

<sup>2</sup> Department of Civil, Environmental and Mechanical Engineering, University of Trento, Via Mesiano 77, 38123 Trento (TN), Italy

<sup>3</sup> Alma Mater Studiorum University of Bologna, Department of Biological, Geological and Environmental Sciences, Via Irnerio 42, 40126 Bologna, Italy; duccio.rocchini@unibo.it

<sup>4</sup> Czech University of Life Sciences Prague, Faculty of Environmental Sciences, Department of Applied Geoinformatics and Spatial Planning, Kamýcka 129, 16500 Prague-Suchbát, Czech Republic

<sup>5</sup> Environmental remote sensing and spectroscopy laboratory (SpecLab), Spanish National Research Council (CSIC), Albasanz 26-28, 28037 Madrid, Spain; mpilar.martin@cchs.csic.es

<sup>6</sup> Department of Ecology, University of Innsbruck, Sternwartestrasse 15, 6020 Innsbruck, Austria; karolina.sakowska@ibe.cnr.it (K.S.); Georg.Wohlfahrt@uibk.ac.at (G.W.)

<sup>7</sup> Institute of BioEconomy, National Research Council (IBE-CNR), Via Biasi 75, 38010 San Michele all'Adige (TN), Italy

<sup>8</sup> Foxlab Joint CNR-FEM Initiative, Via E. Mach 1, 38010 San Michele all'Adige (TN), Italy

\* Correspondence: hafiz.imran@fmach.it; Tel.: +39-389-8921-946

Received: 14 May 2020; Accepted: 9 July 2020; Published: 14 July 2020



**Abstract:** Red-edge (RE) spectral vegetation indices (SVIs)—combining bands on the sharp change region between near infrared (NIR) and visible (VIS) bands—alongside with SVIs solely based on NIR-shoulder bands (wavelengths 750–900 nm) have been shown to perform well in estimating leaf area index (LAI) from proximal and remote sensors. In this work, we used RE and NIR-shoulder SVIs to assess the full potential of bands provided by Sentinel-2 (S-2) and Sentinel-3 (S-3) sensors at both temporal and spatial scales for grassland LAI estimations. Ground temporal and spatial observations of hyperspectral reflectance and LAI were carried out at two grassland sites (Monte Bondone, Italy, and Neustift, Austria). A strong correlation ( $R^2 > 0.8$ ) was observed between grassland LAI and both RE and NIR-shoulder SVIs on a temporal basis, but not on a spatial basis. Using the PROSAIL Radiative Transfer Model (RTM), we demonstrated that grassland structural heterogeneity strongly affects the ability to retrieve LAI, with high uncertainties due to structural and biochemical traits co-variation. The  $RENDVI_{783,740}$  SVI was the least affected by traits co-variation, and more studies are needed to confirm its potential for heterogeneous grasslands LAI monitoring using S-2, S-3, or Gaofen-5 (GF-5) and PRISMA bands.

**Keywords:** leaf area index; grassland; NIR-shoulder indices; Sentinel-2 and Sentinel-3 bands; radiative transfer models

## 1. Introduction

Canopy structural organization describes the three-dimensional geometric distribution of the aboveground photosynthetic and non-photosynthetic vegetation components [1]. Canopy structure is described by plant traits (PTs) such as leaf area index (LAI), aboveground biomass (AGB) and other canopy and leaf structural traits such as leaf angle distribution (LAD), gap fraction, leaf clumping, the proportion of photosynthetic and non-photosynthetic elements [2–4], specific leaf area (SLA) and leaf dry matter, which can influence absorption and scattering light dynamics [5,6].

Remote sensing can provide fundamental spatial and temporal information, which can be used in monitoring PTs related to plant biochemistry, photosynthetic processes and canopy structure. During the last years, the proximal sensing approach was used to fill the scaling gap between leaf and satellite measurements, linking vegetation characteristics and spectral responses from the leaf level to increasing pixel sizes [7–9]. While the visible (VIS) and shortwave infrared (SWIR, 1100–2500 nm) parts of the reflectance spectrum are mainly determined by pigments and water content absorption, respectively, in the near infrared (NIR, 750–1400), reflectance is high compared to the VIS domain because individual leaves and whole plant canopies strongly scatter NIR, and the degree of NIR scattering is driven by the internal leaf structure alongside with canopy structure and the ratio between green and non-photosynthetic components [5].

In herbaceous plants, LAI is a spatially- and temporally-dynamic key trait related to ecosystem functions (e.g., productivity and evapotranspiration), and remote sensing data have been widely used to capture its variability at various scales [10,11]. However, the structural and biochemistry variability among leaves, plants and ecosystems—particularly in natural grasslands, characterized by extreme heterogeneity [9]—is strongly affecting our ability to link spectral variation and LAI. Simultaneously with LAI, factors such as leaf anatomy and LAD are also varying in space and time (e.g., across heterogeneous canopies or due to phenological changes), and this has a significant and often unpredictable impact on scattering across the spectrum. When more structural traits co-vary, LAI estimation based on spectral data may be challenging [5], as reflectance is sensitive to multiple leaf and canopy traits and disentangling LAI from structural and biochemical drivers is difficult [12]. The impact of vegetation structural heterogeneity on the ability of different optical-based models to retrieve LAI has not been sufficiently described in the literature, and new knowledge is needed to quantify the uncertainties of such models and disentangle the impact of structural and biochemical heterogeneity on LAI estimations.

One of the main remote sensing approaches to estimate PTs focuses on empirical models, which are used to quantify relationships between PTs and canopy reflectance or spectral vegetation indices (SVIs) [13,14]. Over the last decades, the SVIs-based methods traditionally used combinations between NIR and VIS bands [15–17] to estimate LAI. However, several authors demonstrated that SVIs based on the NIR and red-edge (RE) spectral domains can significantly improve LAI estimations [13,18,19]. The RE is defined as the spectral region between 680 and 750 nm where a sharp change in the vegetation reflectance can be observed [20–22]. Such spectral domain is on the transition between chlorophyll absorption in the red wavelengths and leaf/canopy scattering in the NIR wavelengths [22,23]. The use of narrow-band SVIs is becoming extremely important in the context of the recently-launched satellite missions such as Sentinel-2 (S-2) and Sentinel-3 (S-3), as well as within the context of new hyperspectral missions such as Gaofen-5 (GF-5) and PRISMA.

The Radiative Transfer Models (RTMs) based on physical principles [24] are capable of simulating the interaction of light with vegetation at leaf and canopy levels and provide an explicit method for estimating the vegetation biophysical variables from canopy reflectance [25]. Another approach to retrieve LAI is based on the inversion of RTM which simulate the interactions of radiation with vegetation elements and the soil [26]. Such inversion approaches demonstrated to be challenging when the model is not well-suited for the observed vegetation type [26] and when suitable ancillary data and regularization methods to optimize the inversions for an efficient parameterization are lacking [27]. In addition, RTMs are mainly focused on chlorophyll and not on other pigments such as brown

pigment content (polyphenols; C<sub>brown</sub>) which play an important role in shaping the spectral response of grasslands at varying phenological stages. This trait is rather poorly analyzed in the literature and the RTM parameter itself lacks of a proper physical meaning, and it is thus not measurable with field observations [28].

### 1.1. Red-Edge and NIR-Shoulder SVIs

Considering the aforementioned RTM limitations and the fact that the new satellite missions are providing several bands across the RE and the NIR shoulder regions, further research is expected on the ability of SVIs based on such regions to retrieve LAI and on the spectral response mechanisms at the canopy level in different vegetation types [29], which are not yet fully explored [30,31]. RE SVIs (which make use of the RE spectral region) include the RE-based normalized difference vegetation index (RENDVI [32]) and the chlorophyll index (CI<sub>re</sub> [33]). These SVIs were found to be very effective in estimating not only canopy chlorophyll content but also LAI [19,34,35].

In recent years, a number of studies have used SVIs combining bands starting from around 750 nm and beyond (750–770 nm) with the NIR bands (“NIR-shoulder SVIs”) for the estimation of LAI and phytomass [36,37]. Vescovo et al. [36] analyzed the performance of normalized infrared difference index (NIDI), calculated using simulated Chris Proba H25 and H18 bands, to estimate phytomass. H25, centered at 872 nm, is a NIR band, while the band H18, centered at 748 nm, lies on the borderline between the RE and the NIR shoulder (750 nm). The NIDI index [36] has been shown to perform well in determining phytomass even for a Mediterranean grassland characterized by a significant presence of brown canopy elements, which suggested a possible chlorophyll-independent nature of the phytomass-index relationship due to wavelength-dependent scattering dynamics. NIR-shoulder SVIs were also used by Liang-yun et al. [37], who demonstrated how the simple ratio of reflectance at 780 and 890 nm can be used for assessing leaf structure features, confirming the ability of NIR-based SVIs to detect the effect of leaf deterioration and senescence.

The SVIs nomenclature regarding the RE and NIR spectral region, unfortunately, is often not consistent. S-2 bands 5, 6 and 7 (respectively, at 705, 740 and 783 nm) are considered to be part of the RE region [38,39] although band 7 is well beyond the threshold between RE and NIR and is in the NIR-shoulder region (750–900 nm [20–22]). In addition, a few authors [9,40,41] using normalized difference indices (NDIs) based on S-2 bands 7 and 8 (or 8a) refer to such SVIs as RENDVI indices, although they only make use of NIR-shoulder bands. The definition of two bands NDIs used in this study is presented in Section 2.3.1.

### 1.2. SVIs and LAI Empirical Models: Does Trait-Covariation Matter?

SVIs combining NIR and RE bands have been used in the last years to estimate both structural and biochemistry-related traits. The impact of structural traits on reflectance in RE spectral regions and on RE SVIs, however, is arousing controversy. According to some authors, RE SVIs are able to reduce structure-related artifacts in retrieved biochemical-related traits, as the RE is thought to be sensitive to chlorophyll content and largely unaffected by structural properties [12]. More recently, Peng et al. [41] showed that SVIs based on NIR band and RE band of 740 nm (RE740) demonstrated to be good predictors of canopy chlorophyll in crop types with contrasting canopy structure. The authors concluded that using NIR and RE740 band combinations provided good chlorophyll estimation due to the “reduced sensitivity of the RE to hysteresis driven by different canopy and leaf structures”. Conversely, many authors agree on the fact that both biochemistry and structure contribute in determining the spectral response also within the RE domain [12,42–44]. At the same time, Ollinger [5] pointed out that the variation in SVIs involving VIS and NIR bands is often driven to a greater extent by the variation in NIR reflectance than by variation in the VIS reflectance. In this context, the impact of canopy structure on SVIs still needs to be clarified.

The aforementioned controversies highlight that the response of structural traits, in combination with biochemical ones, on reflectance and on the SVIs models accuracy has not been fully characterized

for different canopy types. To this regard, more efforts are needed to characterize the spectral response in the RE reflectance domain—in heterogeneous canopies—at varying biochemistry and structure, and more specifically to analyze the impact of canopy structural and leaf traits co-variation on SVIs-LAI relationships [45]. Such characterization is particularly important for multi-species natural grassland canopies, characterized by high spatial heterogeneity and temporal phenological changes, as presented in Section 2.3.4. Darvishzadeh et al. [46] concluded that LAI estimation in grasslands with mixed species and heterogeneous architecture is challenging, and that detailed investigations are needed to assess the suitability of different remote sensing models when many combinations of several species are observed.

In this framework, the objectives of the present study were:

- To compare the ability of different SVIs including information from the RE and the NIR-shoulder spectral regions to estimate LAI at both temporal and spatial scales using ground hyperspectral data
- To analyze the potential of Sentinel band combinations across the RE and the NIR-shoulder spectral regions using S-2 and S-3 simulated bands to estimate LAI in two grassland ecosystems of the Alps with contrasting structures
- To determine the impact of grassland structural and biochemical heterogeneity on LAI estimations by analyzing the spectral reflectance response to co-varying biochemical and structural leaf and canopy traits across the RE and NIR-shoulder spectral domain using an RTM approach
- To identify the best performing S-2 and S-3 SVIs for monitoring grasslands with heterogeneous structure by describing the impact of co-varying leaf and canopy structural traits on the relationships between LAI and SVIs calculated from S-2 and S-3 bands, as well as comparing RTM and empirical approaches.

## 2. Materials and Methods

### 2.1. Study Sites

This study was conducted in two different grassland sites of the Italian and Austrian Alps (Figure 1), situated in the subalpine and montane vegetation belts, respectively, and characterized by contrasting management types.

The first site is a permanent meadow at the Viote del Monte Bondone plateau (46.0147N–11.0458E, Italian Alps). The plateau meadow is managed mostly extensively, with low mineral fertilization and one cut annually around mid-July. In its central part, the meadow hosts a Fluxnet Eddy Covariance (EC) tower (IT-MBo, Italy). Due to its heterogeneous management and orography, the plateau is characterized by the presence of different grassland types characterized by extremely varying LAI and biomass [9]. Such heterogeneous meadows include several different vegetation types (two most abundant associations, one of them including two variants [9]). The *Sievers-Nardetum strictae* association (average aboveground biomass: 236 g·m<sup>-2</sup> [9]) covers a high portion of the plateau, including the EC footprint, and is characterized by short canopies and not intensively managed. The *Scorzonero Aristatae-Agrostidetum tenuis* (average aboveground biomass: 384 g·m<sup>-2</sup>) association is also very common on the plateau; it grows on calcareous soils and includes very productive species, which, although typical of much lower altitudes, can be frequent in some of the most fertile and well-exposed areas of the plateau (e.g., *Arrhenatherum elatius* and *Dactylis glomerata*). The plateau, in its Eastern part, consists of small peatland associations of *Caricion fuscae* and *Caricion davallianae* characterized by very high productivity [9].

At the IT-MBo, several different ecosystems with extremely contrasting structures and productivity can be found within a few hundreds of meters distance (Figure S1). The vegetation in sampling Plots 47 was very tall (maximum height reached 120 cm) and their structure was more erectophile, which is representative of the *Arrhenatherion* alliance considered one of the most common vegetation types of Central Europe, at medium-lower altitudes. Vegetation in Plots 1–3 was very short with small dense *Nardus* tussocks and a limited number of scattered *Festuca* spikes (maximum height

50 cm). These plots represent, in their physiognomy, a typical grassland (meadow or pasture) on lime-deficient or acidified soils from the lower mountains of Europe, up to the lower alpine belt above the timberline. Vegetation in Plots 8–10 showed an intermediate height (maximum 90 cm) and was characterized by the presence of medium-productive grasses (such as *Agrostis Tenuis* and *Trisetum flavescens*) and forbs. This vegetation type is representative of a typical Centro-European species-rich mesophile grasslands at intermediate altitudes (between the *Arrhenatherion* and *Nardus* types) of the montane and sub-alpine levels. The IT-MBo meadow soil can be classified as a Typic Hapludalfs, lyme loamy, mixed, mesic with the following characteristics in the 0–30 cm horizon: total soil organic content (SOC) =  $9.4 \pm 0.4 \text{ kg C m}^{-2}$ ; total N =  $0.29 \pm 0.02 \text{ kg N m}^{-2}$ ; and soil bulk density =  $0.79 \pm 0.29 \text{ g cm}^{-3}$  [47].

The second site (AT-Neu, Fluxnet site) is a meadow located in Neustift (47.1162 N, 11.3204 E, Tyrol, Austria) classified as a *Pastinaco-Arrhenatheretum* [48]. The meadow shows very high productivity (with aboveground biomass values of up to  $700 \text{ g m}^{-2}$  [36]) and is intensively managed with three cuts in mid-June, at the beginning of August and at the end of September. The vegetation type includes a few dominant graminoids (*Dactylis glomerata*, *Festuca pratensis*, *Phleum pratense* and *Trisetum flavescens*) and forbs which are abundant in terms of biomass and are characterized by wider leaves such as *Ranunculus acris*, *Taraxacum officinale*, *Trifolium repens*, *Trifolium pratense* and *Carum carvi* (Figure S2 [48]). The 1-m deep soil profile in AT-Neu meadow soil has been classified as a Fluvisol (FAO classification) with a very thin organic layer (up to 2 cm) and beyond which it is described as a sandy loam. The vegetation roots reach down to 50 cm, but 80% of them are concentrated in the upper 13 cm of the soil [48].

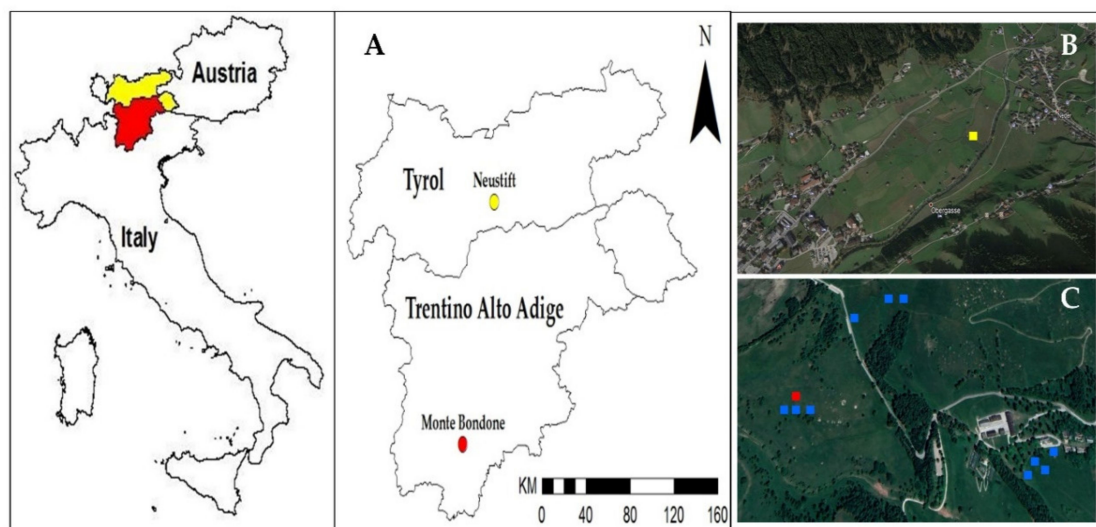


**Figure 1.** Location of the study sites (A); RGB Google Earth image of the AT-Neu site, where the yellow square represents the plot for temporal observations (B); and RGB Google Earth image of the IT-MBo site, where the red square represents the plot for temporal observations, while the blue squares represent the plots for spatial observations (C).

## 2.2. Ground Biophysical Measurements

In the growing season of 2013, the fraction of absorbed photosynthetically active radiation (fAPAR) in IT-MBo was quantified at different vegetation development stages by periodic measurements (8 measurements in the period between May and July 2013) of incoming, reflected and transmitted (2 repetitions) PAR using the SunScan Canopy Analysis System (Delta T Devices Ltd., Cambridge, UK). In 2014, the fAPAR in IT-MBo was estimated using continuous measurements in the period between June and July 2014 by means of the Li-COR PAR sensors (Li-COR Inc., Lincoln, Nebraska, USA). Two Li-190 Quantum sensors were installed above the canopy level, measuring both incoming and

reflected PAR, while the third sensor (Li-191 Line Quantum) was placed at the ground level, measuring PAR transmitted through the vegetation canopy.

The temporal patterns of fAPAR in AT-Neu in the growing season of 2018 were computed using continuous measurements in the period between April and May 2018 carried out with BF2H (Delta T Devices Ltd., Cambridge, UK) and QSO-Sun (Apogee Instruments, Inc., Logan, UT, USA) sensors measuring incoming and reflected PAR, respectively, and two SQ-316 Line Quantum sensors (Apogee Instruments, Inc., Logan, UT, USA) measuring transmitted PAR. In both ecosystems (IT-MBo, AT-Neu), the temporal scale measurements of transmitted PAR with line sensors were performed within the footprint of the ASD-WhiteRef hyperspectral system. All the PAR data were recorded by a data logger (CR3000 in IT-MBo 2014, CR1000 in AT-Neu 2018; Campbell Scientific Inc., Logan, Utah, USA) at 1-min intervals and averaged over solar noon (11:00–13:00 local solar time) to match the time period used for vegetation spectral properties calculations. The spatial patterns of fAPAR in the biomass peak season of 2017 in IT-MBo were quantified at 10 different grassland plots using the SunScan Canopy Analysis System (Delta T Devices Ltd., Cambridge, UK). Two fAPAR measurements were conducted along the transect of the sampling plots with the SunScan instruments, which consist of 64 PAR sensors embedded in a 1-m-long portable probe positioned underneath the grass canopy. In each plot, the probe was positioned along 2 diameter axes (one orthogonal to the other), thus providing  $64 \times 2 = 128$  individual measurements, which were averaged prior to fAPAR calculation. Additionally, two measurements of reflected and incoming light were performed with the probe right above the canopy. The summary of biophysical measurements acquired in the study is presented in Table 1.

**Table 1.** Summary of spectral and biophysical measurements acquired in the study.

Study Site	Year	Observation Period	No. of Observations	Measurement Time Window	Observation Scale	Measurements
IT-MBo	2013	May 2013–July 2013	8	Averaged over solar noon (11:00–13:00 of local solar time)	Temporal	Spectral fAPAR
	2014	June 2014–July 2014	14	Averaged over solar noon (11:00–13:00 of local solar time)	Temporal	Spectral fAPAR
	2017	July 2017	10	Acquisition around solar noon (12:00–14:00 of local solar time)	Spatial	Spectral fAPAR
AT-Neu	2018	April 2018–May 2018	49	Averaged over solar noon (11:00–13:00 of local solar time)	Temporal	Spectral fAPAR

The fAPAR was calculated as:

$$\text{fAPAR} = (\text{PAR}_i - \text{PAR}_r - \text{PAR}_t) \times \text{PAR}_i^{-1} \quad (1)$$

where  $\text{PAR}_i$ ,  $\text{PAR}_r$  and  $\text{PAR}_t$  are incident, reflected and transmitted PAR, respectively.

LAI was estimated non-destructively by an indirect method based on canopy PAR transmission using PAR sensors data and a physical model of radiative transfer “INVERSION” [49]. The model of radiative transfer considers the canopy as a turbid medium in which multiple scattering occurs due to elements of turbidity (phytoelements). The model uses four adjustable parameters: (1) phytoelement dispersion factor; (2) phytoelement reflection; (3) transmission coefficients; and (4) soil reflection. The LAD function for the investigated vegetation type was assumed as erectophile [50], and it was used in “INVERSION” parameter settings. None of the other parameters (dispersion, reflectivity, transmissivity and soil reflectivity) were determined for the investigated canopies, thus default values [49] were used in the model to estimate the LAI.

### 2.3. Hyperspectral Reflectance Measurements

Hyperspectral reflectance data at both sites (in IT-MBo in the growing season of 2013 and 2014 and in AT-Neu in the growing season of 2018) were acquired (Table 1) on a continuous basis by means of the ASD-WhiteRef system [35], allowing measurements in the wavelength range between 350 and 2500 nm. The installation height (6 m in IT-MBo and 2.6 m in AT-Neu) and the system FOV (25 deg) resulted

in an optical canopy footprint diameter of about 2.7 and 1.1 m in IT-MBo and AT-Neu, respectively. Both the ASD-WhiteRef narrow band reflectance spectra were averaged over 2 h close to the solar noon (11:00–13:00 local solar time) to minimize the solar angle effects and then used for computing the SVIs.

In addition, in 2017, spectral observations were performed in the spatial domain in IT-MBo plateau by deploying the ASD FieldSpec Pro spectroradiometer (Analytical Spectral Devices, Inc., Boulder, CO, USA) equipped with a fiber optic with the field of view of 25 deg and a white reference panel on a custom-made aluminum portable system (of a height of 2 m and the resulting FOV of ca. 0.9 m, Figure S3) designed for periodic nadir observations. The portable system consisted of a vertical pole equipped with two horizontal arms (installed one above another; the upper one was fixed and served the fiber optic assembly; the second arm—placed 20 cm below—was rotatable and allowed installation of the white reference panel) enabling alternating observations of the reference and the vegetation target and a ground structure ensuring system stability.

The spatial observations were carried out in July 2017 in 10 different grassland plots covering the aforementioned vegetation types and characterized by quite diverse canopy structure (Figure S1) and productivity [9]. The canopy structure of the investigated grasslands was ranging from very short and dense canopies with *Nardus Stricta* (typical of high altitudes: V1–V3; Figure S1) to very productive grasslands with tall species such as *Dactylis Glomerata* and *Arrhenatherum elatius* (V4–V7; Figure S1). For the spatial observations, the field campaign was conducted at the biomass peak to explore as many plots as possible within a short period (3 days) to avoid grass phenological changes (browning of the vegetation) and to ensure clear-sky conditions. The number of spatial scale observations was in general lower than that of temporal observations, as the latter were carried out on a more continuous basis.

### 2.3.1. Best Band Combination and Hyperspectral NDIs

To identify the band combinations most sensitive to LAI, the normalized difference index ( $NDI = (B1 - B2)/(B1 + B2)$ , where B1 and B2 refer to reflectance values at specific ASD-WhiteRef bands) was calculated with all possible two-band combinations based on ASD ground hyperspectral data within the VIS and NIR spectral range (350–1000 nm) at 1-nm resolution. The definition of the two-band NDIs used in this study is presented in Figure 2. The 2D correlograms for B1 (350–1000 nm) versus B2 (350–1000 nm) highlights the performance of SVIs in the different spectral regions: the VIS region (400–680 nm), the RE region (680–750 nm) and the NIR-shoulder region (750–900 nm). The correlograms were generated using the “Spectral Indices (SI) assessment toolbox” from a modular software package ARTMO (Automated Radiative Transfer Models Operator) [51]. The SI ARTMO toolbox facilitates the assessment of spectral-domain prediction efficiency based on the adopted SI formulation and generates the correlation ( $R^2$ ) matrices with all possible two-band combinations between measured and estimated values for any biophysical parameter [52]. The 2D correlograms illustrate the performance of all two-bands normalized difference combinations in retrieving LAI.

### 2.3.2. Multispectral Sentinel 2 and 3 SVIs

To obtain the reflectance values in the S-2 and S-3 bands, a simulation approach considering the average reflectance over the bandwidth of the respective S-2 and S-3 bands was adopted following Peng et al. [41]. SVIs based on S-2 and S-3 simulated bands (Table S1) in the VIS-NIR, RE and NIR-shoulder spectral regions were calculated, and their potential for estimation of grasslands LAI was tested. Two SVIs ( $NDVI_{865,665}$  and  $MTCI$ ) were based on VIS and NIR reflectance (referred to as VIS-NIR SVIs), three SVIs ( $RENDVI_{783,740}$ ,  $RENDVI_{783,705}$  and  $RENDVI_{865,740}$ ) were based on RE and NIR reflectance (referred to as RE SVIs) and the other two SVIs ( $NSDI_{779,754}$  and  $NSDI_{865,783}$ ) were based on the NIR-shoulder reflectance ( $\geq 750$  nm; referred to as NIR-shoulder SVIs). We chose to compare the performance of two VIS-NIR SVIs (as a reference), alongside the performance of three RE making use of a RE band and two NIR-shoulder indices (Table 2).

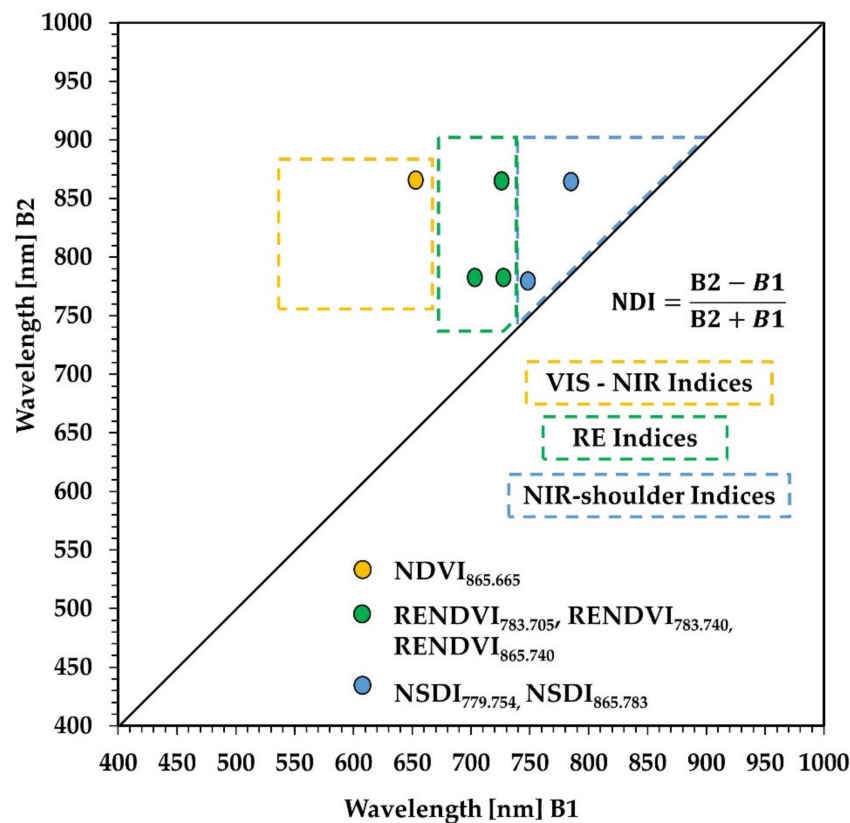


**Figure 2.** VIS-NIR, RE and NIR-shoulder (yellow, green and blue boxes, respectively) band combinations used to calculate normalized difference spectral vegetation indices (NDIs). “ $NDI = (B1 - B2) / (B1 + B2)$ ” represents the general formula for calculating NDIs, where B1 and B2 refer to reflectance at two different bands.

**Table 2.** SVIs based on S-2 and S-3 bands.

SVIs Group	SVIs	Other Names	Formula	References
VIS-NIR	NDVI <sub>865.665</sub>		$(8a - B4) / (8a + B4)$	[15]
	MTCI		$(8a - B5) / (B5 - B4)$	[53]
Red-Edge	RENDVI <sub>783.740</sub>		$(B7 - B6) / (B7 + B6)$	[41]
	RENDVI <sub>783.705</sub>	NDre2	$(B7 - B5) / (B7 + B5)$	[40,41]
NIR-Shoulder	RENDVI <sub>865.740</sub>	NDVire2n	$(8a - B6) / (8a + b6)$	[9,40]
	NSDI <sub>779.754</sub> <sup>1</sup>		$(O16 - O12) / (O12 + O16)$	Proposed in this study
	NSDI <sub>865.783</sub>	NDVire3n	$(8a - B7) / (8a + B7)$	[40]

<sup>1</sup> S-3, simulated index. Fernández-Manso et al. [40] referred to RENDVI<sub>783.705</sub> as Normalized Difference RE 2 (NDre2), RENDVI<sub>865.740</sub> as Normalized Difference Vegetation Index RE 2 narrow (NDVire2n), and NSDI<sub>865.783</sub> as Normalized Difference Vegetation Index RE 3 narrow (NDVire3n).

### 2.3.3. Global Sensitivity Analysis

Different factors (e.g., background soil and Solar-object-sensor geometry parameters) besides the biochemical and structural traits affect the canopy reflectance. To investigate the impact of structural PTs on reflectance, the ARTMO Global Sensitivity Analysis (GSA) toolbox was used [45]. The Variance-based GSA enables evaluating the relative importance of the spectral bands by identifying relative contribution (SI) of the key input variables that drive RTM spectral outputs [49]. The PROSAIL model input parameters used in this study for the GSA analysis are summarized in Table 3. The biochemical and structural input variables of the PROSAIL RTM model co-varied between the minimum and maximum value and for the geometrical parameters used the fixed averaged value.



**Table 3.** Input parameters used in the global sensitivity analysis (GSA). LAI was estimated from the canopy fAPAR measurements at IT-MBo. The ranges of other input parameters (N, Cab, Car, Cw, Cm, Cbrown, soil and LAD) were selected based on existing literature [54–58].

PROSAIL Parameters	Symbol	Unit	Minimum Value	Maximum Value	Avg/Fixed Value
Leaf structural parameter	N	-	1.5	1.9	1.7
Leaf chlorophyll content	Cab	$\mu\text{g cm}^{-2}$	40	70	55
Carotenoid content	Car	$\mu\text{g cm}^{-2}$	3.75	12.65	8.2
Brown pigment	Cbrown	-	0	0.2	0.1
Leaf water content	Cw	$\text{mg cm}^{-2}$	0.01	0.05	0.03
Leaf dry matter	Cm	$\text{mg cm}^{-2}$	0.005	0.01	0.007
<sup>1</sup> Leaf area index	LAI	$\text{m}^2 \cdot \text{m}^{-2}$	0.3	3.7	2
Leaf angle distribution	LAD	(deg)	0	90	45
Hotspot	H	-			0.01
Soil Reflectance	soil	-	0	1	0
Solar zenith angle	$\theta_s$	(deg)			25
Observation zenith angle	$\theta_v$	(deg)			0
Relative Azimuth Angle	$\varphi$	(deg)			0

<sup>1</sup> Estimated from fAPAR field measurements.

#### 2.3.4. SVIs Performance Using Simulated Spectra Under Different Temporal and Spatial Scenarios

RTMs are used to understand light interception by plant canopies and for the interpretation of vegetation reflectance in terms of biophysical characteristics [54]. In this study, the PROSAIL RTM [52] was used to assess the influence of leaf and canopy PTs on the SVIs calculated based on VIS, RE and NIR-shoulder spectral regions. PROSAIL couples two separate models: (a) the PROSPECT leaf optical model; and (b) the SAIL canopy reflectance model [28]. PROSAIL can simulate the canopy bidirectional reflectance in the spectral range between 400 and 2500 nm as a function of up to 16 input parameters. In this study, the input parameters were constrained according to the ranges of biophysical parameters measured in the field and literature-based values (Table 3). A look-up table (LUT) generated using the Latin hypercube sampling (LHS) method [59] was adopted to achieve a uniform distribution of the model inputs within the given boundaries for each scenario. The LHS method divides the cumulative density function into  $n$  bins of the same size from which data are randomly selected.

To investigate the impact of structural (LAI, LAD, leaf structural parameter (N) and leaf dry matter (Cm)) and biochemical (leaf chlorophyll content (Cab), carotenoid content (Car), brown pigment content (Cbrown) and leaf water content (Cw)) input parameters of PROSAIL on canopy spectral reflectance, various scenarios were assumed.

Using co-variation between input variables to constrain the model, we adopted parameters ranges observed in the literature (Table 3). With this approach, we aimed at exploring the impact of traits co-variation at both the spatial scale (due to vegetation heterogeneity) and the temporal scale (due to grassland phenological changes). Hence, running PROSAIL with a 100-iteration step, we analyzed four scenarios (1t–4t) based on the LAI range observed at the temporal scale at IT-MBo (during the growing period), as follows:

(1t) LAI was set to vary between the minimum (at the beginning of the season) and the maximum value (at the biomass peak) and other PROSAIL parameters were kept constant (average value). This corresponds to a theoretical scenario where only grassland canopy LAI changes during the growth period, and no change is assumed in both other canopy structural parameters and biochemistry.

(2t) LAI and LAD values were co-varying between the minimum and the maximum value (Table 4) during the growth period and the rest of the PROSAIL parameters were kept constant (average value). This scenario can be considered representative of grasslands with slight canopy architectural and leaf structural dynamics at different growth stages.

(3t) LAI, LAD, N and Cm values were co-varying between the minimum and the maximum value (Table 4) and the rest of the PROSAIL parameters (Table 3) were kept constant at the average value. This corresponds to a scenario where all canopy and leaf structural traits change during the growing season (due to, e.g., ecological factors such as temperature, soil moisture and light competition), but biochemical traits remain constant. This scenario can be associated with grasslands where phenology, species composition and management practices (e.g., architectural changes due to variation of species composition after mowing and leaf biochemical changes due to fertilization) are determining more evident both canopy architectural and leaf structural traits dynamics at the temporal scale.

(4t) All the PROSAIL input variables (Table 4) were allowed to co-vary from the minimum to the maximum value. This corresponds to a scenario where there is a relevant temporal co-variation of both canopy structural and biochemical traits. Such scenario can be considered representative of grasslands with more extreme phenology dynamics, due to: (i) stronger changes of ecological factors related to climate dynamics and water availability (e.g., in Mediterranean grasslands with strong seasonal variations of leaf water content, leaf chlorophyll content and proportion of brown dead leaves); or (ii) management practices (e.g., architectural changes due to variation of species composition after mowing and leaf biochemical changes due to fertilization).

The PROSAIL model was also run with a 100-iteration step for four scenarios (1s–4s) using the range of LAI measured during spatial observations (minimum and maximum values measured in the field at the biomass peak) as an input parameter (Table 4) as follows:

(1s) LAI was set to vary between the minimum (in the less productive grassland) and the maximum value (in the most productive grassland) and other PROSAIL parameters were kept constant at their average value. This corresponds to a theoretical scenario where grassland is spatially homogeneous in terms of both structure and biochemistry.

(2s) LAI and LAD values were set to vary between the minimum and the maximum value and other PROSAIL parameters (Table 4) were kept constant (average value). This scenario can be considered representative of grasslands with slightly spatially-heterogeneous species composition and functional types.

(3s) LAI, LAD, N and Cm values were co-varying between the minimum and the maximum value and other biochemical parameters were kept constant. This scenario corresponds to a grassland with strong structural spatial heterogeneity, while biochemistry is homogeneous. It can be associated with grasslands with heterogeneous species composition and functional types, associated with spatial variation of ecological factors (e.g., soil moisture and pH, topographic aspect, etc.).

(4s) All the PROSAIL parameters were co-varying. This scenario corresponds to a grassland with strong structural and biochemistry spatial heterogeneity and can be considered representative of grasslands with extreme variations of species composition, plant functional types, ecological factors and management regimes.

All PROSAIL simulations were performed using the MATLAB environment (The MathWorks Inc. 2019a).

### 2.3.5. Statistical Analysis

To compare the performance of the investigated NDIs in LAI estimation, the following linear and second-order polynomial regression statistics were computed:  $R^2$ , coefficient of determination; Adj.  $R^2$ , adjusted coefficient of determination; and RMSE, root mean square error. All statistical analyses were performed by means of the R software (version 3.6.0, <https://www.r-project.org/>).

**Table 4.** Different scenarios analyzed with the PROSAIL simulation at the temporal (1t–4t) and spatial (1s–4s) scales.

PROSAIL Simulation Scenarios	1t/1s	2t/2s	3t/3s	4t/4s
<b>Scenarios at the Temporal Scale (1t–4t)</b>	LAI varying between minimum and maximum values (temporal scale field observations)	LAI co-varying between minimum and maximum values (temporal scale field observations) LAD: 0–90	LAI co-varying between minimum and maximum values (temporal scale field observations) LAD: 0–90 N: 1.5–1.9 Cm: 0.005–0.01	All PROSAIL parameters co-varied.
<b>Scenarios at the Spatial Scale (1s–4s)</b>	LAI varying between minimum and maximum values (spatial scale field observations)	LAI co-varying between minimum and maximum values (spatial scale field observations) LAD: 0–90	LAI co-varying between minimum and maximum values (spatial scale field observations) LAD: 0–90 N: 1.5–1.9 Cm: 0.005–0.01	All PROSAIL parameters co-varied.

### 3. Results

#### 3.1. Relationship between the Measured Spectra and LAI

Temporal trends of LAI in IT-MBo (2013 and 2014) and in AT-Neu (2018) are shown in Figure 3A–C, respectively. Figure 3D presents LAI corresponding to spatial observations. For temporal scale observations, the values of LAI at IT-MBo ranged from 0.3 to 3.7, while, at AT-Neu, LAI ranged from 0.2 to 8.8 and showed a smoother LAI increase compared to IT-MBo. At the spatial scale in IT-MBo, as the measurements were carried out at the biomass peak, the variability was lower and the LAI ranged from 2.0 to 4.5.

The canopy reflectance obtained from field measurements performed at different vegetation growth stages is plotted in Figure 3A–C (IT-MBo 2013, IT-MBo 2014 and AT-Neu 2018, respectively), while reflectance spectra obtained from spatial scale measurements (IT-MBo 2017) are displayed in Figure 3D. In the case of temporal observations, canopy reflectance showed a typical response to LAI increase, mostly characterized by a gradually decreasing reflectance in the VIS region, a gradually increasing reflectance in the NIR-shoulder region and increasing NIR-shoulder slope as observed by Vescovo et al. [36]. On the contrary, the reflectance values of spatial scale observations at IT-MBo 2017 showed a much more complex pattern (Figure 3D), where increasing values of LAI did not always result in higher NIR and lower visible reflectance. As an example, the grassland plot highlighted in yellow (with a relatively high LAI value of 3.4) had a very low NIR reflectance, while the grassland plot highlighted in red (LAI 4.5, corresponding to the highest LAI value) showed the highest reflectance in the visible wavelengths.

The reflectance values at 740 nm appeared to be relatively closer to the ones of the NIR shoulder plateau at AT-Neu 2018 compared to IT-MBo 2013, IT-MBo 2014 and IT-MBo 2017, suggesting a lower chlorophyll absorption at this wavelength in this ecosystem. The NIR-shoulder slope, between 760 and 900 nm, observed in AT-Neu 2018 was generally slightly less steep compared to the slope observed in IT-MBo in both temporal and spatial scale observations.

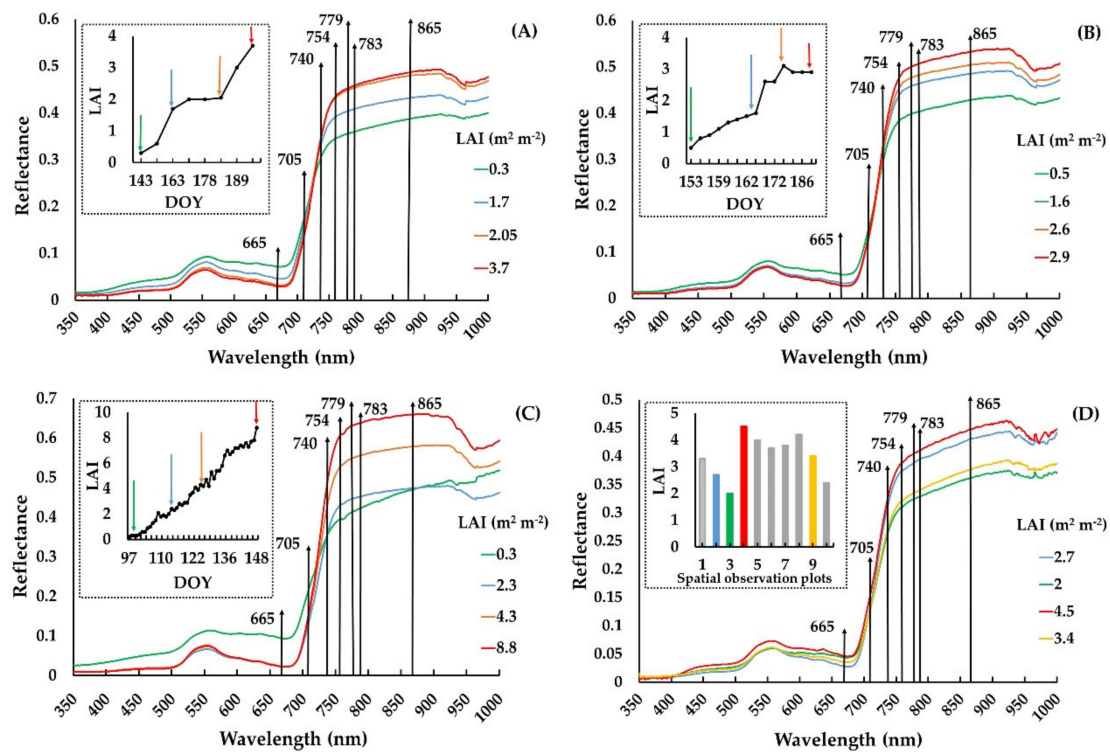


**Figure 3.** Reflectance spectra at different growth stages measured in the field at: IT-MBo 2013 (A); IT-MBo 2014 (B); and AT-Neu 2018 (C); and spectra from spatial observations at IT-MBo 2017 (D).

### 3.2. Best Band Combination and Hyperspectral NDIs

Figure 4 shows the  $R^2$  resulting from the linear regression between LAI and two-band combinations of reflectance values from 350 to 1000 nm using hyperspectral data. The correlograms based on temporal observations from IT-MBo (2013 and 2014) and AT-Neu (2018) provided a clear overview of the optimal band combinations for retrieving LAI. In the case of IT-MBo temporal observations (Figure 4A,B), the  $R^2$  values displayed very consistent patterns across VIS-NIR band combinations, but with slightly different  $R^2$  ranges for both investigated years: the maximum  $R^2$  was around 0.8 for IT-MBo 2013 and 0.9 for IT-MBo 2014 and the minimum  $R^2$  was slightly higher for IT-MBo 2013 compared to IT-MBo 2014. At the AT-Neu study site, generally lower  $R^2$  values were observed compared to the IT-MBo temporal observations. In the VIS spectral region, a slightly different pattern of the  $R^2$  values was observed for both study sites (Figure 4C). The  $R^2$  patterns were more different across the RE and NIR-shoulder regions. In particular, an evident shift of the well-correlated areas towards the lower wavelengths (from around 750 nm to 740 nm) was observed for AT-Neu (Figure 4C) compared to IT-MBo temporal observations (Figure 4A,B).

All the two bands NDIs (Table 2) showed high  $R^2$  values for temporal scale observations at IT-MBo ( $R^2 > 0.75$ ,  $\text{NDVI}_{865,665}$ ,  $\text{RENDVI}_{783,740}$ ,  $\text{RENDVI}_{783,705}$ ,  $\text{RENDVI}_{865,740}$  and  $\text{NSDI}_{779,754}$  in Figure 4A,B), except for the  $\text{NSDI}_{865,783}$  index ( $R^2 < 0.3$ , Figure 4A,B). For AT-Neu, a slightly different pattern of  $R^2$  values was observed, where  $\text{RENDVI}_{865,740}$  and  $\text{NSDI}_{779,754}$  showed very low correlations compared to IT-MBo ( $R^2 > 0.2$ , Figure 4C). The best correlations at the AT-Neu site were observed for the  $\text{RENDVI}$  NDIs ( $\text{RENDVI}_{783,740}$  and  $\text{RENDVI}_{783,705}$ ) with  $R^2$  values exceeding 0.6 (Figure 4A–C). Therefore, the  $\text{RENDVI}_{783,740}$ , which is still not very commonly used in the literature, performed well at both sites. Although the NIR-shoulder  $\text{NSDI}_{779,754}$  showed a significant correlation with high  $R^2$  values ( $R^2 > 0.85$  Figure 4A,B) at the IT-MBo site, much lower  $R^2$  values were observed for the same band combinations at At-Neu ( $R^2 < 0.2$ , Figure 4C).

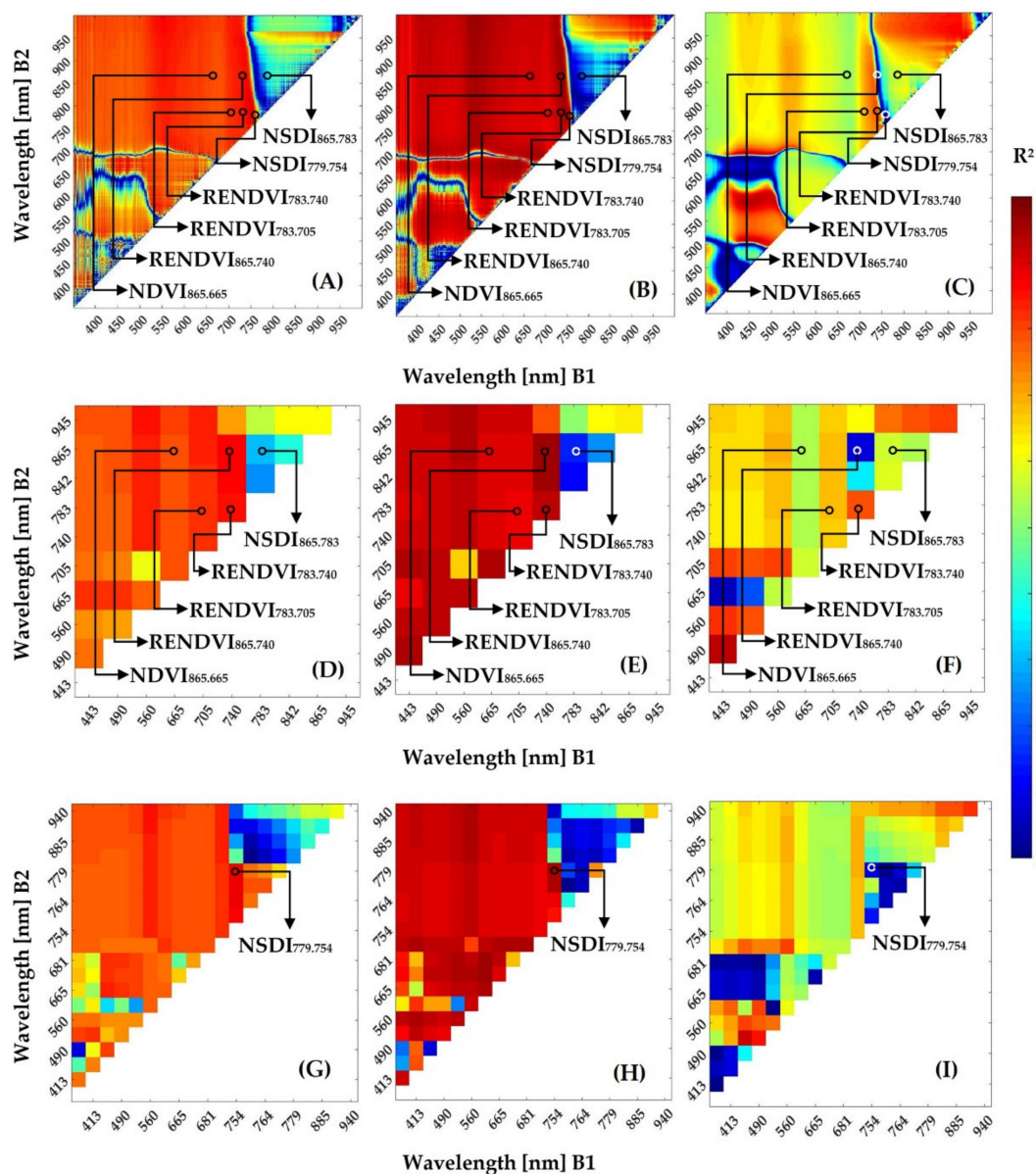


**Figure 4.**  $R^2$  values based on linear regression between the normalized difference of all two-band combinations and LAI for both study sites (IT-MBo 2013 (A); IT-MBo 2014 (B); and AT-Neu 2018 (C)) considering the temporal scale hyperspectral observations.  $R^2$  obtained using: (A–C) the hyperspectral data; (D–F) S-2 simulated bands; (G–I) S-3 simulated bands. Black/white circles refer to the position of the indices in the correlogram and arrows are indicating the name of the respective indices.

Other than the aforementioned SVIs, there is a wide range of band combinations which showed a strong correlation with LAI. For both sites, an area of high  $R^2$  values ( $R^2 > 0.7$ ) was observed for combinations within the NIR part of the spectrum (B2 around 950–970 nm and B1 of 900–950 nm; Figure 4A–C). Such band combinations are commonly used to calculate water band SVIs which are indicators of water status [60–64]. On the other hand, water band SVIs demonstrated to be good proxies of structure-related parameters such as LAI and phytomass [10,65]. A strong correlation between Normalized Water Index (NWI; calculated with PRISMA bands B2 of 962 nm and B1 of 897 nm [62,63,66]) and LAI was observed ( $R^2$  value for IT-MBo 2013 = 0.77, for IT-MBo 2014 = 0.83 and for AT-Neu 2018 = 0.85).

The correlogram based on S-2 (Figure 4D–F) and S-3 (Figure 4G–I) bands provides an overview of the performance of band combinations obtained with the average reflectance over the bandwidth of

the respective S-2 and S-3 bands. For both study sites, the S-2 graph indicated that the RENDVI based on wavelength 740 and 783 nm is among the best correlated with LAI ( $R^2 > 0.65$ , Figure 4D–F). For S-3 simulated data, NSDI<sub>779,754</sub> showed very high correlations for IT-MBo ( $R^2 > 0.75$ , Figure 4G,H) but very low correlations at AT-Neu. Moreover, we also analyzed the correlograms of RMSE based on temporal observations (Figure S4), showing that the RMSE patterns were mostly similar but inverse, as high  $R^2$  values corresponded with low RMSE values and vice versa.

Results from the observations at the spatial scale at IT-MBo 2017 showed poorer correlations (Figure 5A) than those obtained with the multi temporal data. Only band combinations from the spectral range within 350–400 nm showed slightly higher  $R^2$  values compared to the rest of the band combinations. The correlograms of RMSE based on spatial observations presented in Figure S5 showed overall high RMSE for most of the two band combinations.

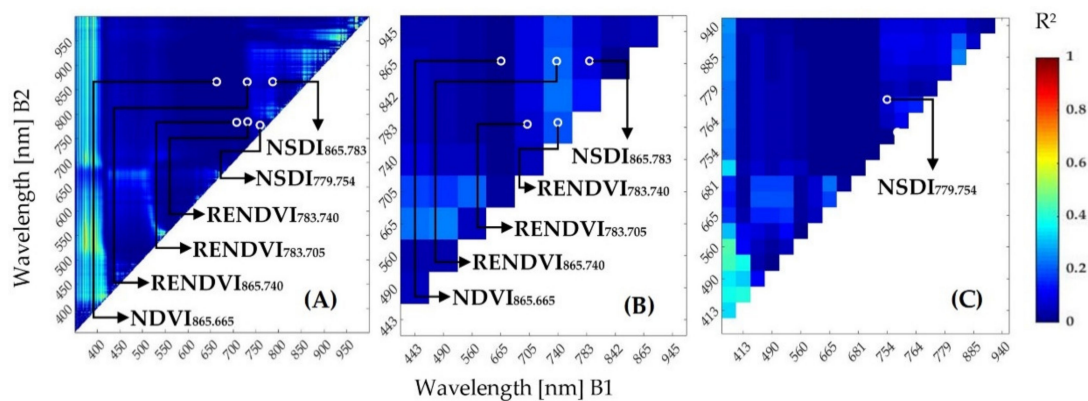


**Figure 5.**  $R^2$  values based on linear regression between the normalized difference of all two-band combinations and LAI for IT-MBo 2017 considering the spatial scale observations: (A)  $R^2$  obtained using the hyperspectral data; and (B,C)  $R^2$  obtained using S-2 and S-3 simulated bands, respectively. White circles refer to the position of the indices in the correlogram and arrows are indicating the name of the respective indices.

### 3.3. The Performance of Multispectral Sentinel 2 and 3 SVIs

Scatterplots between VIS-NIR SVIs (calculated with data resampled to S-2 bands) and LAI for both sites are presented in Figure 6. Both investigated VIS-NIR SVIs (NDVI<sub>865,665</sub> and MTCI) showed a high correlation with an  $R^2 > 0.75$  and  $RMSE < 0.5 \text{ m}^2 \cdot \text{m}^{-2}$  (Figure 6A,B and Table 5) for observations on a temporal basis at IT-MBo. For the AT-Neu study site (which has very high productivity and LAI values up to 8.8), NDVI<sub>865,665</sub> showed a strong saturation effect (Figure 6A) compared to MTCI, resulting in a lower  $R^2$  value ( $R^2 = 0.55$  and  $R^2 = 0.81$  for NDVI<sub>865,665</sub> and MTCI, respectively) and RMSE ( $RMSE = 1.71 \text{ m}^2 \cdot \text{m}^{-2}$  and  $RMSE = 1.11 \text{ m}^2 \cdot \text{m}^{-2}$ , respectively). Conversely, when considering the observations at the spatial scale performed at IT-MBo, no significant correlation was found between the investigated VIS-NIR SVIs and LAI (Figure 6C,D and Table 5).

Scatterplots between RE-based SVIs (calculated with data resampled to S-2 bands) and LAI for both sites are presented in Figure 7. The  $R^2$  values of the linear relationship between RE SVIs and LAI in IT-MBo were high with  $R^2 > 0.8$  (up to 0.96 and  $RMSE < 0.45 \text{ m}^2 \cdot \text{m}^{-2}$ ) for the temporal observations at IT-MBo, but at the AT-Neu site the RE SVIs showed slightly lower  $R^2$  ( $< 0.8$  with  $RMSE > 1 \text{ m}^2 \cdot \text{m}^{-2}$ ) values, as a result of the saturation effect (Table 5). The saturation effect was particularly strong for NDVI<sub>865,665</sub> and for AT-Neu site, where a polynomial regression model showed to increase the  $R^2$  from 0.55 to 0.71 and decrease RMSE from 1.71 to 1.37  $\text{m}^2 \cdot \text{m}^{-2}$ . For all other SVIs, polynomial relationships showed only a slight increase of the performance of the model (Table S2). The RE SVIs including RENDVI<sub>783,740</sub> and RENDVI<sub>783,705</sub> from temporal scale observations showed a strong correlation with an  $R^2 > 0.65$  for both study sites, but RENDVI<sub>865,740</sub> lost its predictive power at AT-Neu ( $R^2 = 0.2$  and

RMSE = 2.28 m<sup>2</sup>·m<sup>-2</sup>). As for VIS-NIR SVIs, the observations at the spatial scale showed very low R<sup>2</sup> (< 0.06) values.

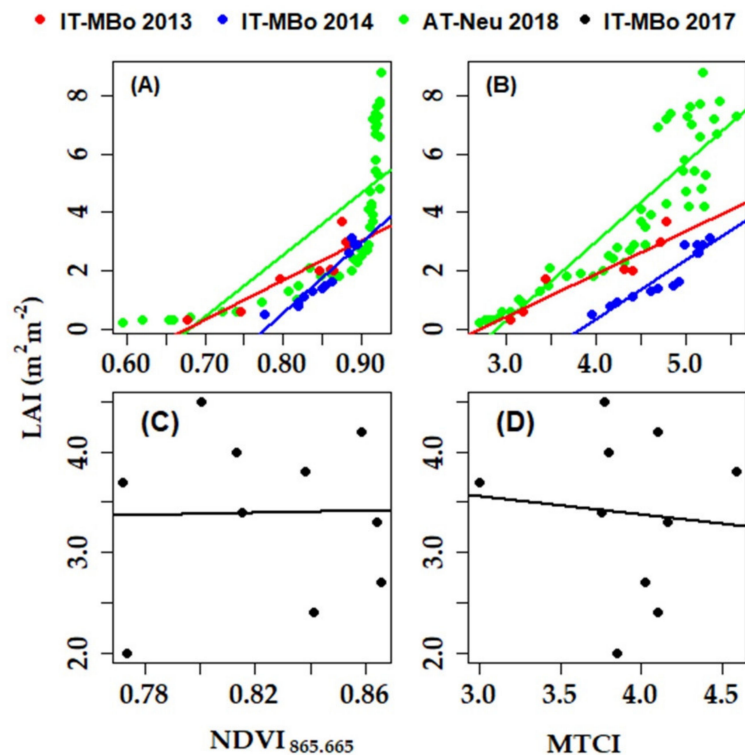


**Figure 6.** Relationship between VIS-NIR indices and LAI: for temporal observations at IT-MBo (2013 and 2014) and AT-Neu 2018 (A,B); and for spatial observations at IT-MBo 2017 (C,D). In all panels, solid lines represent a linear fit to the data.

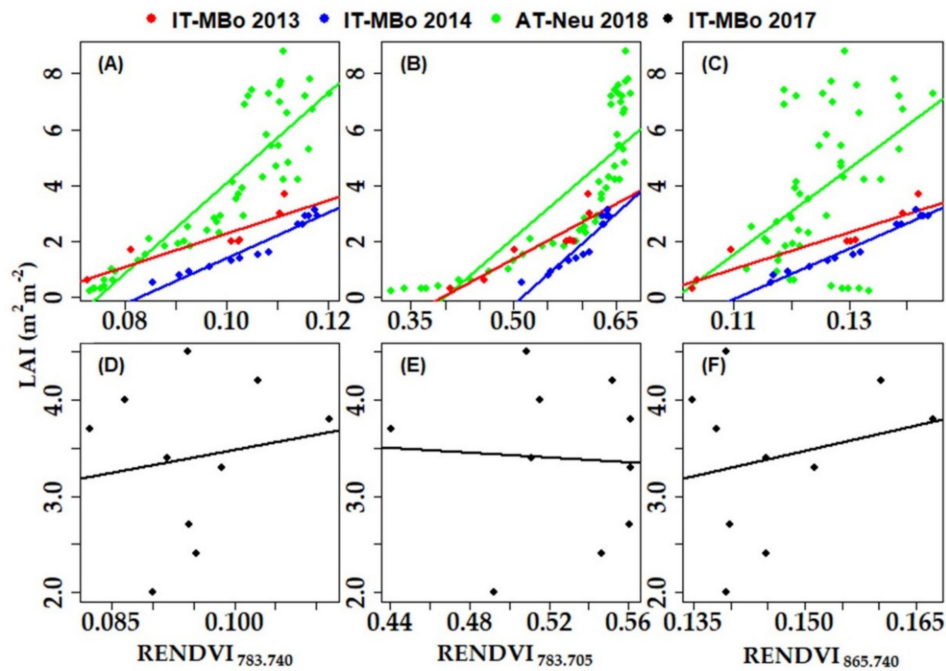


**Figure 7.** Relationship between RE indices and LAI: for temporal observations at IT-MBo (2013 and 2014) and AT-Neu 2018, respectively (A–C); and for spatial observations at IT-MBo 2017 (D–F). In all panels, solid lines represent a linear fit to the data.

Concerning the NIR shoulder SVIs, the  $NSDI_{779.754}$  showed a strong positive correlation with an  $R^2 > 0.8$  (up to 0.95 and  $RMSE < 0.40 \text{ m}^2 \cdot \text{m}^{-2}$ ) for the temporal observations at IT-MBo, but at the AT-Neu study site the correlation was much weaker ( $R^2 < 0.1$ , Figure 8A;  $RMSE = 2.44 \text{ m}^2 \cdot \text{m}^{-2}$ , Table 5). The index based on 865 and 783 nm showed an inverse relationship with LAI for both ecosystems, with weaker correlation at IT-MBo ( $R^2 < 0.3$ ) compared to AT-Neu ( $R^2$  of 0.58, Figure 8B). No significant correlations were observed on the spatial basis (Figure 8C,D).

Considering all the VIS-NIR, RE and NIR shoulder SVIs,  $RENDVI_{783.740}$  was always among the three best-performing SVIs, for observations carried out at the temporal scale at the two investigated sites (Table 5). The other SVIs with good performance at the temporal scale were  $RENDVI_{865.740}$ , MTCI and  $NSDI_{779.75}$ .

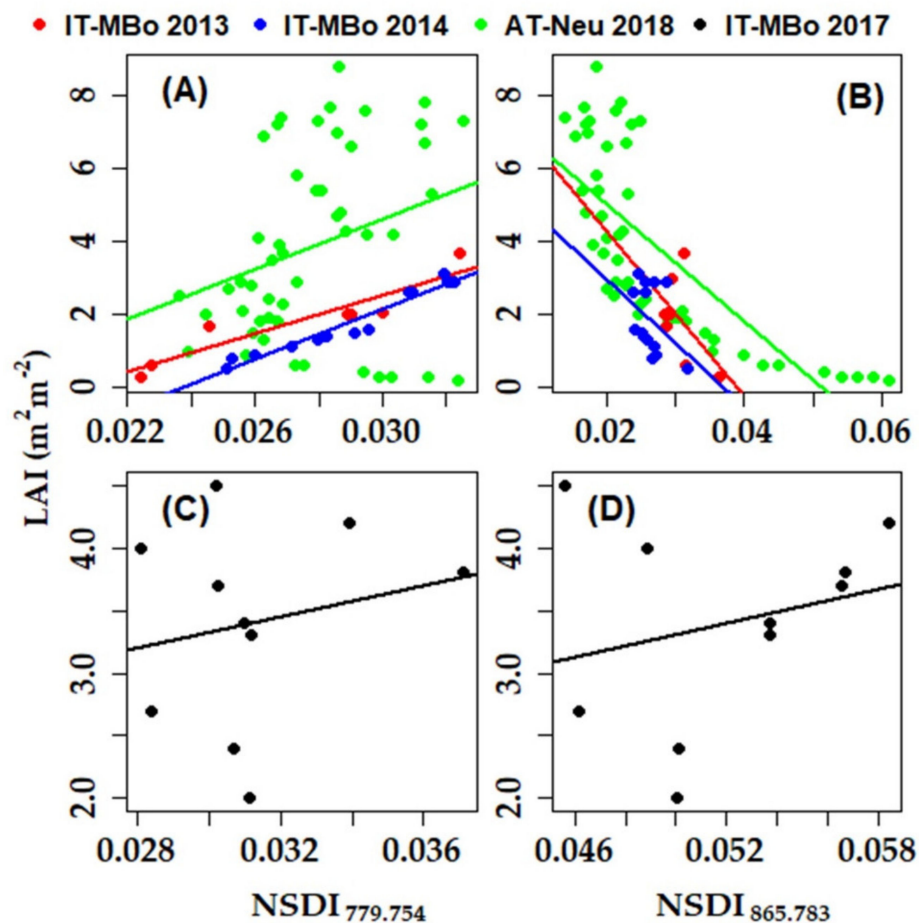


**Figure 8.** Relationship between NIR-shoulder indices and LAI: for temporal observations at IT-MBo (2013 and 2014) and AT-Neu 2018, respectively (A,B); and for spatial observations at IT-MBo 2017 (C,D). In all panels, solid lines represent a linear fit to the data.



**Table 5.** Summary of the statistics (N, Number of observations;  $R^2$ , coefficient of determination; Adj.  $R^2$ , adjusted coefficient of determination; RMSE, root mean square error) of the linear regression between leaf area index (LAI,  $m^2 \cdot m^{-2}$ ) estimated from fraction of absorbed photosynthetically active radiation (fAPAR) and the spectral vegetation indices (SVIs) calculated from measured spectra for IT-MBo 2013, IT-MBo 2014 and AT-Neu 2018 at temporal scale observations and for IT-MBo 2017 at spatial scale observations. The three best-fitting models are highlighted in bold. Asterisk indicates significance of correlation: \*\*\*  $p < 0.001$ ; \*\*  $p < 0.01$ ; \*  $p < 0.05$ . n.s., not significant (Pearson's correlation test).

SVIs	Temporal Scale Observation									Spatial Scale Observations		
	IT-MBo 2013 (N = 8)			IT-MBo 2014 (N = 14)			AT-Neu 2018 (N = 49)			IT-MBo 2017 (N = 10)		
	$R^2$	Adj. $R^2$	RMSE ( $m^2 \cdot m^{-2}$ )	$R^2$	Adj. $R^2$	RMSE ( $m^2 \cdot m^{-2}$ )	$R^2$	Adj. $R^2$	RMSE ( $m^2 \cdot m^{-2}$ )	$R^2$	Adj. $R^2$	RMSE ( $m^2 \cdot m^{-2}$ )
<b>VIS-NIR</b>												
NDVI <sub>865.665</sub>	0.79 **	0.76	0.48	0.90 ***	0.90	0.27	0.55 ***	0.54	1.71	0.00 n.s.	−0.12	0.77
MTCI	0.83 **	0.81	0.43	0.87 ***	0.86	0.32	<b>0.81 ***</b>	<b>0.81</b>	<b>1.11</b>	0.01 n.s.	−0.12	0.77
<b>Red-Edge (RE)</b>												
RENDVI <sub>783.740</sub>	<b>0.85 **</b>	<b>0.83</b>	<b>0.40</b>	<b>0.93 ***</b>	<b>0.93</b>	<b>0.23</b>	<b>0.79 ***</b>	<b>0.78</b>	<b>1.18</b>	0.03 n.s.	−0.09	0.76
RENDVI <sub>783.705</sub>	0.82 **	0.79	0.44	0.89 ***	0.88	0.30	<b>0.67 ***</b>	<b>0.66</b>	<b>1.47</b>	0.00 n.s.	−0.12	0.77
RENDVI <sub>865.740</sub>	<b>0.86 **</b>	<b>0.83</b>	<b>0.39</b>	<b>0.96 ***</b>	<b>0.96</b>	<b>0.17</b>	0.20 **	0.18	2.28	0.05 n.s.	−0.06	0.75
<b>NIR-Shoulder</b>												
×NSDI <sub>779.754</sub>	<b>0.88 **</b>	<b>0.86</b>	<b>0.37</b>	<b>0.95 ***</b>	<b>0.95</b>	<b>0.20</b>	0.09 *	0.07	2.44	0.04 n.s.	−0.08	0.75
NSDI <sub>865.783</sub>	0.28 n.s.	0.16	0.89	0.15 n.s.	0.07	0.82	0.58 ***	0.57	1.66	0.06 n.s.	−0.06	0.75

### 3.4. Global Sensitivity Analysis of the Spectral Bands

The results concerning the impact of leaf and canopy parameters on the different spectral regions through the GSA are illustrated in Figure 9. Background (soil) demonstrated to have a rather homogeneous impact on canopy reflectance across all wavelengths. LAI and Cab demonstrated a major influence on reflectance in the VIS part of the spectrum and Cab showed two SI peaks (around 560 and 705 nm) and an impact on the reflectance response was observed up to 760 nm. Within the RE (680–750 nm) part of the spectrum, the influence of LAD was significantly increasing at longer wavelengths, with SI reaching about 40% at 740 nm, while at 705 nm the SI was less than 10%. For spectral bands in the RE region, a slight effect of Cbrown and Cm was also observed, while the impact of LAI was significantly increasing from RE to NIR-Shoulder spectral bands. LAI and LAD were the main drivers of reflectance also in the far RE region (740–750 nm) of the spectrum. Within the NIR-shoulder region (750–900 nm), reflectance showed to be driven mostly by LAI and LAD, while Cm showed an average SI value of less than 5%. In the spectral range 740–820 nm, Cbrown also showed SI values up to 5%. Leaf water content (Cw) response only started beyond 930 nm (Figure 9).

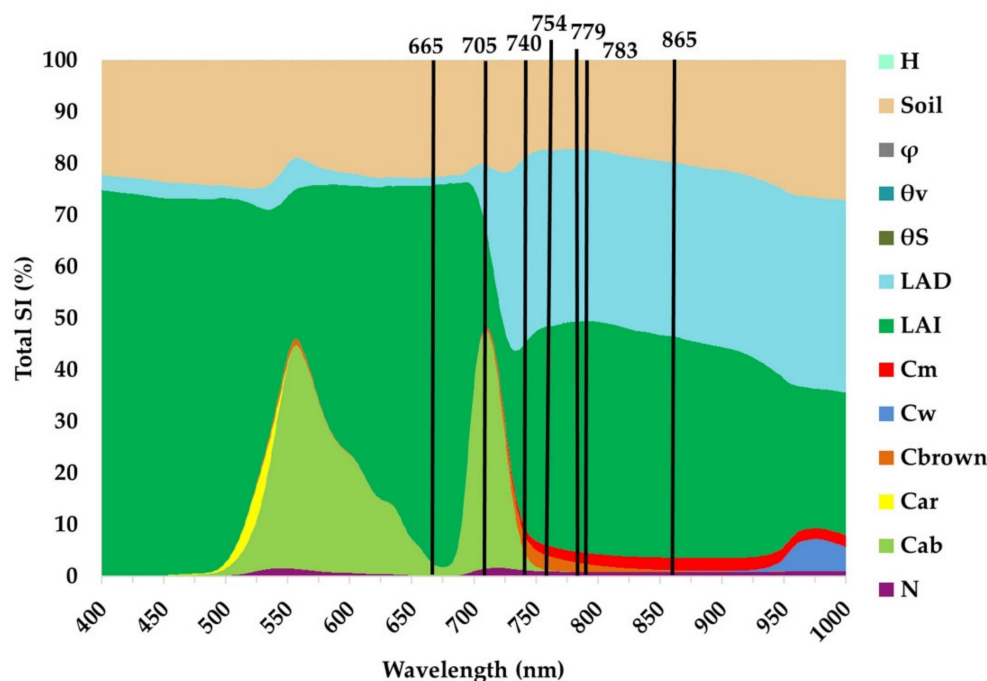


**Figure 9.** Global Sensitivity Analysis of the PROSAIL input parameters. The dimension of the sensitivity refers to the relative contribution (SI) of each input variable and the vertical bars represent the positions of the bands (solid lines, S-2; dotted lines, S-3) used to calculate the investigated SVIs. Input parameter ranges, full names of the variables and units are presented in Table 3.

### 3.5. SVIs Calculated from Modeled PROSAIL Reflectance Simulations vs. LAI

To analyze the impacts of co-variation of structural and biochemical traits for LAI monitoring using the PROSAIL modeled reflectance output, a series of scatterplots between the SVIs and LAI is presented in this section. The modeled reflectance was obtained from PROSAIL simulations constraining the input parameters according to the eight scenarios presented in Section 2.3.4.

For the investigated grasslands at IT-MBo, the LAI range observed at the temporal scale also included low LAI values (0.3), while the minimum LAI value for spatial scale observations was 2.0. In general, when LAI values were restricted to the spatial range, the lack of low LAI had a strong effect on the predictive power of VIS-NIR SVIs with a noticeable decrease in correlation coefficients when two or more traits were co-varying (Figure 10B–D F for  $NDVI_{865,665}$  and Figure 10F–H for MTCI) and increase in RSME (Tables 6 and 7).

When only LAI was varying (Scenarios 1t and 1s; Figure 10A,E), a high correlation between LAI and VIS-NIR SVIs (NDVI<sub>865.665</sub> and MTCI) was observed; however, NDVI<sub>865.665</sub> ( $R^2 = 0.73$  and  $R^2 = 0.86$  for Scenarios 1t and 1s, respectively) showed a strong saturation effect compared to MTCI ( $R^2 = 0.98$  and  $R^2 = 0.97$  for Scenario 1t and 1s respectively). When it was assumed that LAI and LAD were co-varying, the  $R^2$  values of both NDVI<sub>865.665</sub> and MTCI decreased, but at different rates. In case of NDVI<sub>865.665</sub>, the  $R^2$  decreased to 0.56 (Scenario 2t) and 0.18 (Scenario 2s), while for MTCI the  $R^2$  dropped to 0.95 (Scenario 2t) and 0.85 (Scenario 2s). Similarly, in Scenario 3t, MTCI performed significantly better (Figure 10G,  $R^2 = 0.85$ , Table 6) than NDVI<sub>865.665</sub> (Figure 10C,  $R^2 = 0.52$ , Table 6); however, a noticeable decrease of  $R^2$  was observed in the correspondent spatial scenario for MTCI ( $R^2 = 0.43$ , Table 7). Scenario 4t (all PROSAIL input parameters co-varied) resulted in a slight increase—compared to Scenario 3t—in  $R^2$  values between NDVI<sub>865.665</sub> and LAI (Figure 10D,  $R^2 = 0.57$ , RSME =  $0.81 \text{ m}^2 \cdot \text{m}^{-2}$  (Scenario 4t), Table 6; and  $R^2 = 0.19$ , RSME =  $0.65 \text{ m}^2 \cdot \text{m}^{-2}$  (Scenario 4s), Table 7). On the other hand, MTCI showed very low  $R^2$  values (Figure 10H,  $R^2 = 0.39$ , RMSE =  $0.97 \text{ m}^2 \cdot \text{m}^{-2}$  (Scenario 4t), Table 6; and  $R^2 = 0.11$ , RSME =  $0.68 \text{ m}^2 \cdot \text{m}^{-2}$  (Scenario 4s), Table 7).

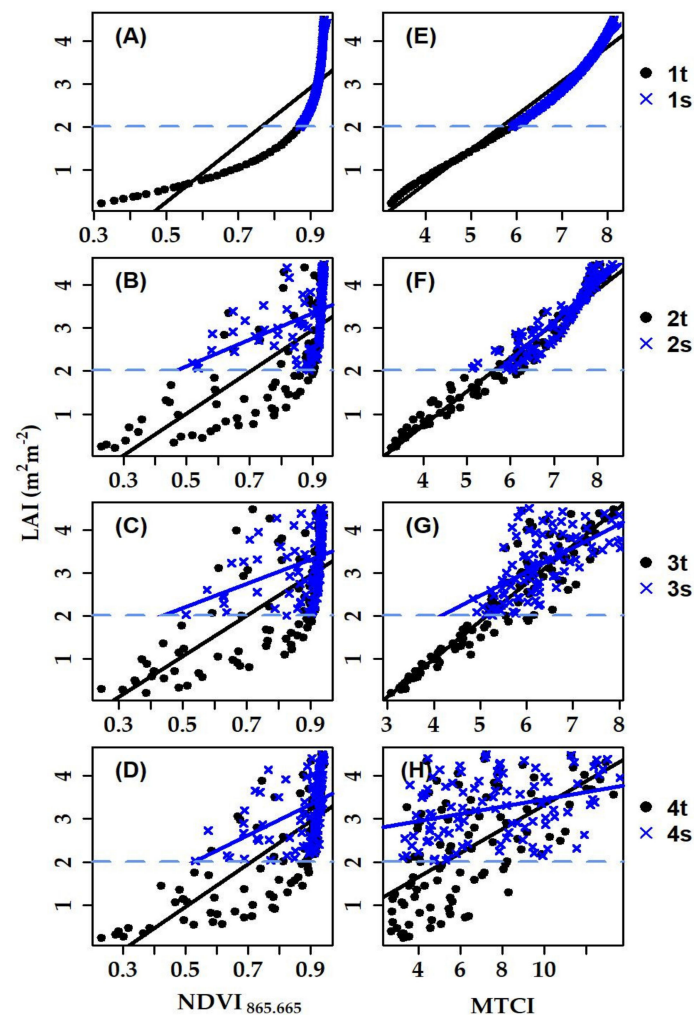


**Figure 10.** Relationships between VIS-NIR indices and LAI for all eight scenarios for both temporal ((A,E) 1t; (B,F) 2t; (C,G) 3t; and (D,H) 4t) and spatial scale observations ((A,E) 1s; (B,F) 2s; (C,G) 3s; and (D,H) 4s). The horizontal dashed line represents the minimum value of LAI when PROSAIL was run using spatial observation LAI ranges as input parameter. In all panels, solid lines represent a linear fit to the data.

In Figure 11, scatterplots between RE SVIs ( $\text{RENDVI}_{783.740}$ ,  $\text{RENDVI}_{783.705}$  and  $\text{RENDVI}_{865.740}$ ) and LAI are presented. In general, RE SVIs showed a better performance compared to VIS-NIR SVIs for both temporal and spatial scenarios. In Scenarios 1t and 1s, a high correlation between LAI and RE SVIs ( $\text{RENDVI}_{783.740}$  and  $\text{RENDVI}_{865.740}$ ) was observed (Figure 11A,I,  $R^2 > 0.9$ ;  $\text{RSME} < 0.3 \text{ m}^2 \cdot \text{m}^{-2}$ , Tables 6 and 7).  $\text{RENDVI}_{783.740}$  showed to be less sensitive to structural traits co-variation and showed a strong correlation (Figure 11C,  $R^2 = 0.90$ ,  $\text{RSME} = 0.40 \text{ m}^2 \cdot \text{m}^{-2}$  and  $R^2 = 0.62$ ,  $\text{RSME} = 0.45 \text{ m}^2 \cdot \text{m}^{-2}$  for Scenarios 3t and 3s, respectively).  $\text{RENDVI}_{783.740}$  and  $\text{RENDVI}_{783.705}$  SVIs showed the highest correlation with LAI in Scenario 4t (Figure 11D,H,  $R^2 = 0.64$ ,  $\text{RSME} = 0.75 \text{ m}^2 \cdot \text{m}^{-2}$  and  $R^2 = 0.62$ ,  $\text{RSME} = 0.76 \text{ m}^2 \cdot \text{m}^{-2}$ , Table 6). However, even if they were among the best performing indices in Scenario 4t, they lost most of their predictive power in Scenario 4s (Figure 11D,H,  $R^2 = 0.22$ ,  $\text{RSME} = 0.64$  and  $R^2 = 0.21$ ,  $\text{RSME} = 0.64$ , Table 7).

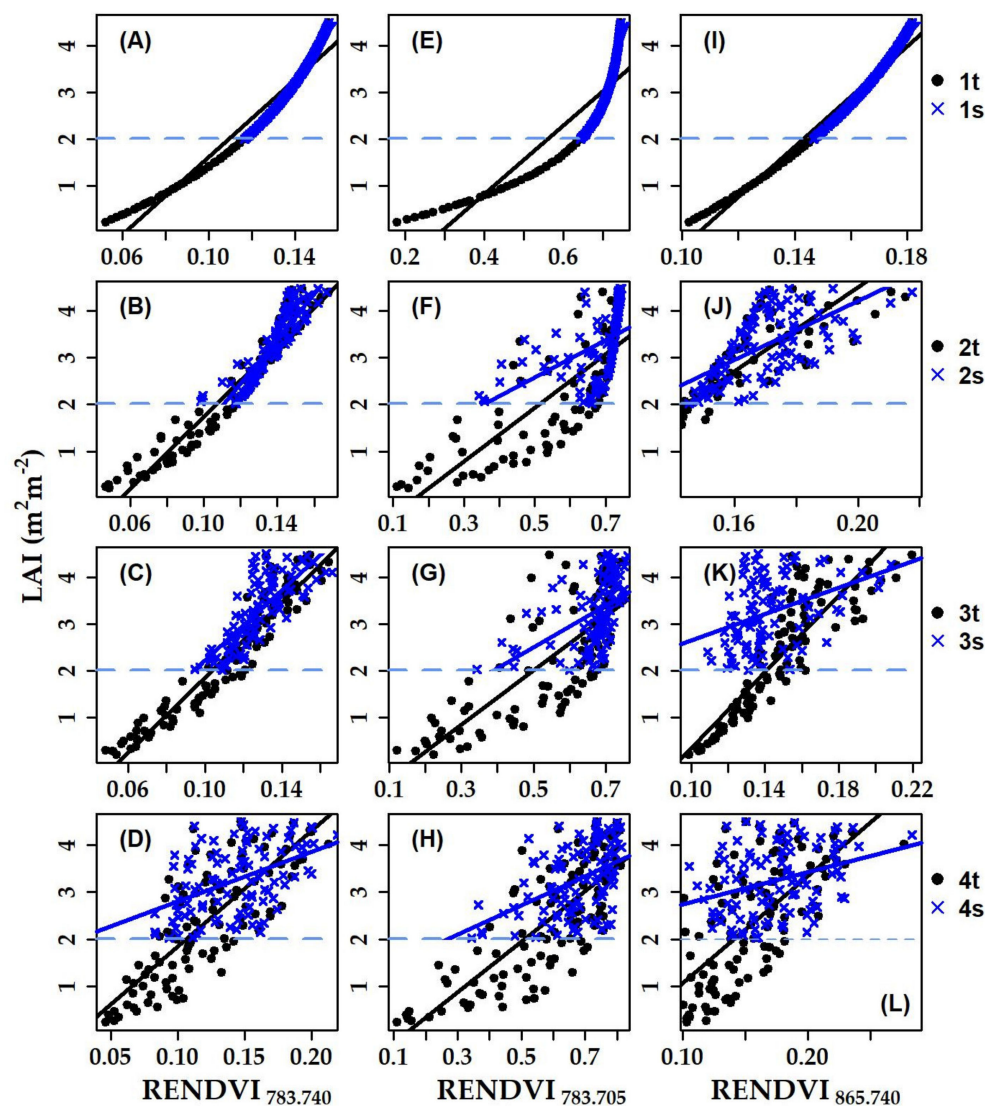


**Figure 11.** Relationships between RE indices and LAI for all eight scenarios for both temporal ((A,E,I) 1t; (B,F,J) 2t; (C,G,K) 3t; and (D,H,L) 4t) and spatial scale observations ((A,E,I) 1s; (B,F,J) 2s; (C,G,K) 3s; and (D,H,L) 4s). The horizontal dashed line represents the minimum value of LAI when PROSAIL was run using spatial observation LAI ranges as input parameter. In all panels, solid lines represent a linear fit to the data.

Similar to RE-based SVIs, the NIR-shoulder ( $\text{NSDI}_{779.754}$ ) showed to mitigate the saturation effect for higher LAI values as observed in Figure 12A–D. In Scenarios 1t and 1s,  $\text{NSDI}_{779.754}$  exhibited a

strong correlation ( $R^2 = 0.99$ ; Figure 12A) and  $RMSE < 0.2 \text{ m}^2 \cdot \text{m}^{-2}$  (Tables 6 and 7). In Scenarios 2t and 3t,  $NSDI_{779,754}$  showed a slight decrease in  $R^2$  value (Figure 12B,C,  $R^2 = 0.93$  and  $0.86$  for Scenarios 2t and 3t respectively) and a noticeable decrease for Scenarios 2s and 3s was observed (Figure 12B,C,  $R^2 = 0.65$  (Scenario 2s) and  $R^2 = 0.33$  (Scenario 3s)). The  $NSDI_{865,783}$  showed an inverse relationship with LAI and showed a low  $R^2 = 0.2$  and  $0.05$  (Figure 12H) for Scenarios 4t and 4s, respectively.

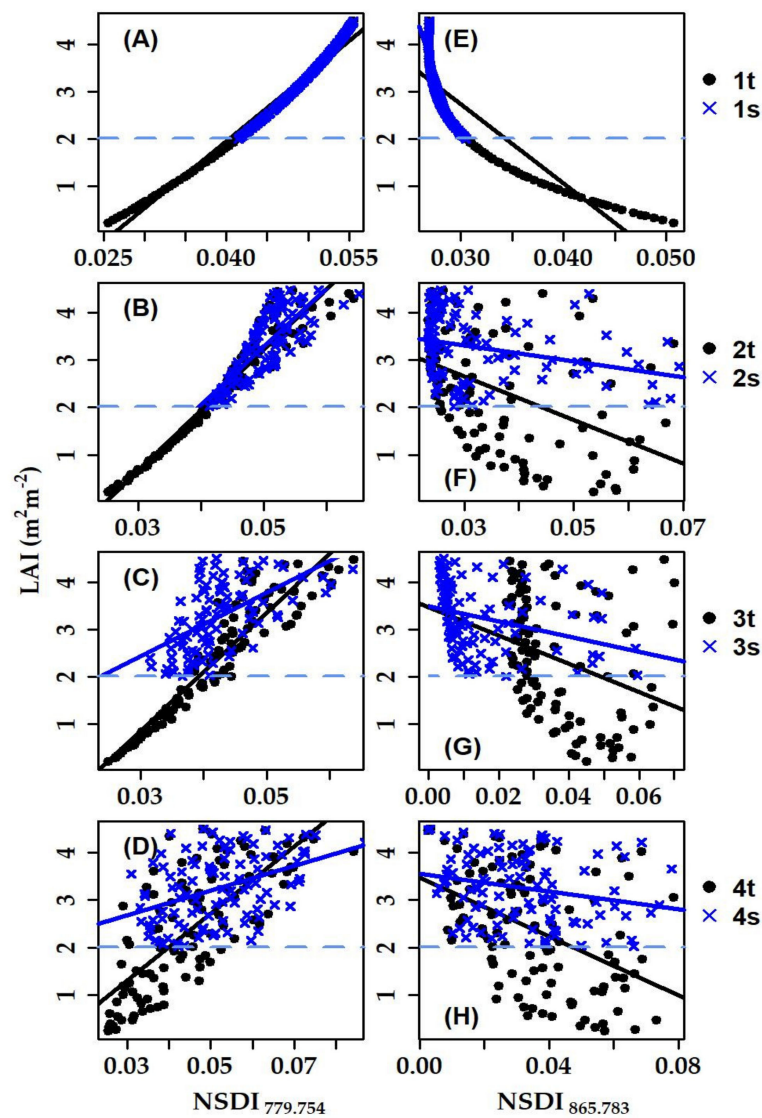


**Figure 12.** Relationships between NIR-shoulder indices and LAI for all eight scenarios for both temporal ((A,E) 1t; (B,F) 2t; (C,G) 3t; and (D,H) 4t) and spatial scale observations ((A,E) 1s; (B,F) 2s; (C,G) 3s; and (D,H) 4s). The horizontal dashed line represents the minimum value of LAI when PROSAIL was run using spatial observation LAI ranges as input parameter. In all panels, solid lines represent a linear fit to the data.

Across the temporal scenarios,  $RENDVI_{783,740}$  was among the three best-performing SVIs when two or more traits were co-varying, while at the spatial scale scenarios,  $RENDVI_{783,740}$  was always among the three best-performing SVIs (Tables 6 and 7, respectively). The other SVIs with good performance across temporal and spatial scenarios were  $NSDI_{779,75}$  and MTCL.

**Table 6.** Summary of the statistics (N, number of observations;  $R^2$ , coefficient of determination; Adj.  $R^2$ , adjusted coefficient of determination; RMSE, root mean square error) of the linear regression between leaf area index (LAI,  $m^2 \cdot m^{-2}$ ) of 100 iteration step between minimum and maximum range of temporal scale measurements and the spectral vegetation indices (SVIs) calculated from PROSAIL simulated spectra by scenarios considering spatial scale LAI ranges (1t–4t) described in Section 2.3.4. The three best-fitting models are highlighted in bold. Asterisk indicates significance of correlation: \*\*\*  $p < 0.001$ ; \*\*  $p < 0.01$ ; \*  $p < 0.05$ . n.s., not significant (Pearson’s correlation test).

SVIs	Scenario 1t, 2t, 3t, 4t											
	1t (N = 100)			2t (N = 100)			3t (N = 100)			4t (N = 100)		
	$R^2$	Adj. $R^2$	RMSE ( $m^2 \cdot m^{-2}$ )	$R^2$	Adj. $R^2$	RMSE ( $m^2 \cdot m^{-2}$ )	$R^2$	Adj. $R^2$	RMSE ( $m^2 \cdot m^{-2}$ )	$R^2$	Adj. $R^2$	RMSE ( $m^2 \cdot m^{-2}$ )
<b>VIS-NIR</b>												
NDVI <sub>865.665</sub>	0.73 ***	0.72	0.65	0.56 ***	0.56	0.82	0.52 ***	0.51	0.86	0.57 ***	0.57	0.81
MTCI	<b>0.98 ***</b>	<b>0.97</b>	<b>0.20</b>	<b>0.95 ***</b>	<b>0.95</b>	<b>0.26</b>	<b>0.85 ***</b>	<b>0.84</b>	<b>0.49</b>	0.39 ***	0.38	0.97
<b>Red-Edge (RE)</b>												
RENDVI <sub>783.740</sub>	0.95 ***	0.95	0.27	<b>0.93 ***</b>	<b>0.93</b>	<b>0.34</b>	<b>0.90 ***</b>	<b>0.90</b>	<b>0.40</b>	<b>0.64 ***</b>	<b>0.63</b>	<b>0.75</b>
RENDVI <sub>783.705</sub>	0.81 ***	0.81	0.54	0.65 ***	0.65	0.73	0.60 ***	0.60	0.78	<b>0.62 ***</b>	<b>0.62</b>	<b>0.76</b>
RENDVI <sub>865.740</sub>	<b>0.98 ***</b>	<b>0.98</b>	<b>0.18</b>	0.87 ***	0.87	0.45	0.77 ***	0.77	0.59	0.44 ***	0.43	0.93
<b>NIR-Shoulder</b>												
×NSDI <sub>779.754</sub>	<b>0.99 ***</b>	<b>0.99</b>	<b>0.15</b>	0.93 ***	0.93	0.32	<b>0.86 ***</b>	<b>0.86</b>	<b>0.46</b>	<b>0.56 ***</b>	<b>0.55</b>	<b>0.83</b>
NSDI <sub>865.783</sub>	0.79 ***	0.79	0.56	0.20 ***	0.19	1.11	0.10 **	0.09	1.18	0.20 ***	0.19	1.11

**Table 7.** Summary of the statistics (N, number of observations;  $R^2$ , coefficient of determination; Adj.  $R^2$ , adjusted coefficient of determination; RMSE, root mean square error) of the linear regression between leaf area index (LAI,  $m^2 \cdot m^{-2}$ ) of 100 iteration step between minimum and maximum range of temporal scale measurements and the spectral vegetation indices (SVIs) calculated from PROSAIL simulated spectra by scenarios considering spatial scale LAI ranges (1s–4s) described in Section 2.3.4. The three best-fitting models are highlighted in bold. Asterisk indicates significance of correlation: \*\*\*  $p < 0.001$ ; \*\*  $p < 0.01$ ; \*  $p < 0.05$ . n.s., not significant (Pearson’s correlation test).

SVIs	Scenario 1s, 2s, 3s, 4s											
	1s (N = 100)			2s (N = 100)			3s (N = 100)			4s (N = 100)		
	$R^2$	Adj. $R^2$	RMSE ( $m^2 \cdot m^{-2}$ )	$R^2$	Adj. $R^2$	RMSE ( $m^2 \cdot m^{-2}$ )	$R^2$	Adj. $R^2$	RMSE ( $m^2 \cdot m^{-2}$ )	$R^2$	Adj. $R^2$	RMSE ( $m^2 \cdot m^{-2}$ )
<b>VIS-NIR</b>												
NDVI <sub>865.665</sub>	0.86 ***	0.86	0.27	0.18 ***	0.17	0.65	0.13 ***	0.12	0.67	<b>0.19 ***</b>	<b>0.18</b>	<b>0.65</b>
MTCI	0.97 ***	0.97	0.12	<b>0.85 ***</b>	<b>0.85</b>	<b>0.28</b>	<b>0.43 ***</b>	<b>0.42</b>	<b>0.55</b>	0.11 ***	0.10	0.68
<b>Red-Edge (RE)</b>												
RENDVI <sub>783.740</sub>	<b>0.98 ***</b>	<b>0.98</b>	<b>0.09</b>	<b>0.82 ***</b>	<b>0.82</b>	<b>0.31</b>	<b>0.62 ***</b>	<b>0.61</b>	<b>0.45</b>	<b>0.22 ***</b>	<b>0.21</b>	<b>0.64</b>
RENDVI <sub>783.705</sub>	0.92 ***	0.92	0.21	0.27 ***	0.26	0.62	0.24 ***	0.23	0.63	<b>0.21 ***</b>	<b>0.21</b>	<b>0.64</b>
RENDVI <sub>865.740</sub>	<b>0.99 ***</b>	<b>0.99</b>	<b>0.07</b>	0.38 ***	0.38	0.57	0.15 ***	0.14	0.67	0.10 **	0.09	0.68
<b>NIR-Shoulder</b>												
×NSDI <sub>779.754</sub>	<b>0.99 ***</b>	<b>0.99</b>	<b>0.06</b>	<b>0.65 ***</b>	<b>0.65</b>	<b>0.42</b>	<b>0.33 ***</b>	<b>0.32</b>	<b>0.59</b>	0.18 ***	0.17	0.65
NSDI <sub>865.783</sub>	0.80 ***	0.80	0.32	0.08 **	0.07	0.69	0.10 **	0.09	0.69	0.05 **	0.04	0.70

#### 4. Discussion

The grassland spectral response across different spectral regions (VIS, RE and NIR-shoulder) showed to be both site-specific and scale-dependent. The NIR-shoulder slope showed different trends at two sites confirming the results of Vescovo et al. [36] on the site-specificity of NIR-shoulder indices. Moreover, the NIR-shoulder slope response at the spatial scale appeared to be more complex than the one at the temporal scale and did not strictly follow the typical temporal response at increasing LAI, characterized by an increase of NIR-shoulder slope corresponding to an increase of LAI.

The importance of using hyperspectral and superspectral sensors adopting SVIs with bands in the RE and NIR shoulder spectral region [19,36] to estimate canopy structure was highlighted in this study for montane temperate grassland ecosystems, and novel band combinations were explored. RTM observations demonstrated that chlorophyll absorption can determine the spectral response well beyond 700 nm, and thus the optimal band combinations to estimate LAI often included far red bands (as shown also in [32,33,67]). Ollinger's paradox [5] stating that (as chlorophyll absorption range was assumed by this author to be 400–700 nm) "the physiological activity of vegetation is often more strongly related to reflectance at wavelengths that are not used in photosynthesis than to those that are" has been—at least partially—explained during the last years as many studies have been highlighting that photosynthetic pigments' absorption is active in the far red domain. In our study, the RTM models indicate that chlorophyll absorption can be observed up to 760 nm (Figure 9), while in vivo observations previously indicated 740 nm as an upper limit [67]. For both sites, high  $R^2$  values were detected for band combinations used in water indices. Such result is opening interesting perspectives as these indices can be calculated using both PRISMA and GF-5 satellite data.

The GSA showed that the VIS part of the spectrum is mainly influenced by LAI and Cab, in the RE spectral region reflectance is determined by LAI, Cab, LAD, Cm and Cbrown. In previous studies the RE spectral region showed optimal performances in retrieving LAI and canopy chlorophyll content. The RE part of the spectrum is characterized by lower absorption by chlorophyll, but remains sensitive to changes in its content, reducing the saturation effect and enhancing the sensitivity of these SVIs to moderate-high vegetation densities reducing the typical SVI saturation effect [32,41]. The evident shift of the well-correlated areas towards the lower wavelengths at the AT-Neu site suggests that the performance of some of the RE SVIs is site-specific, probably partly due to different absorption thresholds [29,36]. It is interesting to notice that, despite such shift, the area corresponding to  $\text{RENDVI}_{783,740}$  was well correlated at both sites, and for both the two years of observations at IT-MBo.

Very contrasting results were achieved at the temporal and spatial scales. At IT-MBo temporal scale strong correlations ( $R^2 > 0.8$ ) were observed between LAI and both traditional RE and NIR-shoulder ( $\text{NSDI}_{779,754}$ ) SVIs. Differently from previous studies [20,36,37], the performance of such indices at the spatial scale was particularly poor with an  $R^2 < 0.1$ . Such poor performance could be partially explained by the different LAI ranges at the temporal and spatial scales. At the spatial scale, saturation of some SVIs may be observed above certain LAI values, and this can constrain the ability to retrieve LAI when only full-canopy cover ecosystems are observed [10]. The poor performance of the SVIs in retrieving LAI at the spatial scale observations is noteworthy and confirming the observations of Dong et al. [68] on the strong response of canopy reflectance to canopy structural traits. Darvishzadeh et al. [46] showed that LAI, in heterogeneous grasslands, could be estimated at the spatial scale using the SVIs approach with intermediate accuracy ( $R^2_{cv}$  values from 0.49 to 0.69). Atzberger et al. [25] evaluated the PROSAIL RTM suitability for grasslands and demonstrated that PROSAIL is well suited for LAI estimations. However, in their study, the PROSAIL-generated and the in-situ hyperspectral-derived correlation plots, across the RE and NIR-shoulder ranges, demonstrated different  $R^2$  patterns between observed and modeled LAI, indicating that RTM parameterization for LAI retrieval is challenging in these spectral domains. The selection of leaf structural and canopy architectural settings is key to achieve an accurate LAI retrieval, and can be complex when heterogeneous canopies are modeled. Following the indications of Darvishzadeh et al. [46] on the impact of grassland species composition and canopy architecture on remote sensing models, we hypothesized that the structural heterogeneity

of the investigated montane temperate grasslands at the spatial scale might play a crucial role on LAI retrieval. Our results confirm that: (i) the co-variation of all structural traits (such as LAI, LAD, Cm and N, at the spatial scale) could explain the poor performance of most SVIs; and (ii) due the co-variation of both structural and biochemistry traits, no SVI is able to provide reliable LAI spatial estimations. In our study, we used the PROSAIL RTM in forward mode to study the impact of co-variation of PTs on LAI estimation. The PROSAIL results confirmed that trait-covariation resulting from extreme grassland heterogeneity has a strong impact on LAI estimation accuracy. Such findings agree with the observations of Ollinger [5] on “the difficulty of assessing the relative importance of individual traits that co-vary with a suite of plant properties”. For the investigated montane temperate grasslands types—characterized by extreme spatial heterogeneity—structural and biochemical intraspecific drivers linked to heterogeneous canopy species composition seem to have a stronger impact on traits estimation than interspecific drivers related to phenology. In other ecosystem types (e.g., arid and Mediterranean grasslands characterized by strong seasonality and extreme phenology dynamics due to changes of ecological factors related to climate and water availability) observations at the temporal scale are more challenging and significant limitations for remote sensing analysis are posed. In such grasslands, senescence can take place at varying rates and periods, increasing the variability of surface biophysical and optical properties [69].

RENDVI<sub>783,740</sub> showed a good performance and it is not very commonly used in the literature, as it was introduced relatively recently. Peng et al. [41] demonstrated that RENDVI<sub>783,740</sub> was accurate in estimating canopy chlorophyll in crops with contrasting architectures (maize and soybean). Our results show how RENDVI<sub>783,740</sub> can be used to monitor grassland LAI. RENDVI<sub>783,740</sub> demonstrated to be the most insensitive to grassland structural traits co-variation. For this reason, considering the increasing availability of hyperspectral and superspectral sensors such as S-2, GF-5 and PRISMA, more studies are needed to investigate its full potential for monitoring grasslands and other spatially-heterogeneous ecosystems.

The impact of structural PTs on the relationships between SVIs and LAI, although is well known in the literature, should be taken more carefully into account [70]. Structural traits directly determine the interactions between light and both leaf and canopy elements. In particular, LAD (which is a key canopy trait whose effect has usually not been considered when applying common vegetation SVIs for mapping LAI) showed to have a strong influence for wavelengths > 705 nm. The impact of LAD has been determined for crops [71], but limited research was carried out for grasslands [36].

Grassland canopy structure heterogeneity may impact the applicability of algorithms to detect vegetation changes due to phenology also at the temporal scale [72,73], and this could be the case of temperate grasslands where species composition and coverage is varying due to, e.g., light competition dynamics. As the co-variation of biochemical traits was included in the PROSAIL RTM simulations, a significant impact on the models accuracy was observed, indicating that both structural and biochemical factors play a major role in models' performance. Biochemical heterogeneity can be determined not only by different vegetation types at the spatial scale, but also by phenological changes. In Mediterranean grasslands, where severe droughts and grassland curing are taking place during the summer months, both biochemical and structural changes are expected [74,75].

Using a combination of two NIR bands (both beyond 750 nm), the NIR-shoulder SVI NSDI<sub>779,75</sub> (calculated from S-3 simulated bands) performed very well at IT-MBo, but not at the AT-Neu. This is probably due to the fact that chlorophyll absorption threshold is different at the two grassland ecosystems, and absorption is still present at 754 nm only in the IT-MBo grassland. This result is defining the green-dependency of NIR shoulder SVIs investigated in Vescovo et al. [36], which were thought to be related to scattering mechanisms and not chlorophyll absorption. Our study highlighted that this spectral region, which has been poorly investigated in the literature, is largely affected, in addition to chlorophyll until 760 nm, by LAI, LAD, Cbrown and Cw.

The suitability of well-known and widely adopted SVIs for retrieving LAI in grasslands with heterogeneous structure was also questioned in this paper. Many widely-adopted SVIs, e.g., NDVI<sub>865,665</sub>



and MTCI, exhibited a strong correlation with LAI when only a few traits were co-varying, while a much weaker correlation was observed when more traits were co-varied. This agrees with the findings of Peng et al. [41] and Horler et al. [22] and advises to carefully evaluate potential uncertainties of satellite-based vegetation products such as LAI, fAPAR in spatially-heterogeneous canopies. In our work, we demonstrated that SVIs such as  $RENDVI_{783,740}$  seem to be less influenced by canopy architecture, leaf structure and biochemical traits co-variation, and need further testing.

In this work, some constraints were highlighted on the use of statistical approaches based on SVIs. However, strong limitations of RTM inversion are also implied, and a reliable LAI spatialization in heterogeneous canopies needs to be based, in the future, on more detailed parameterization of the traits which are co-varying with LAI. RTM models show evident intrinsic limitations in their capacity to simulate heterogeneous canopies [76,77], and do not take fully into account some parameters, e.g., the presence of non-photosynthetic material in the canopy [58]. Furthermore, the GSA showed the impact of many different input parameters on LAI retrieval, and only very preliminary information on the spectral impact of some RTM parameters (e.g., canopy brown pigments and anthocyanins) is available in the literature [76,78].

## 5. Conclusions

The potential of Sentinel bands combinations across the RE and the NIR-shoulder spectral region such as  $RENDVI_{783,740}$  and  $NSDI_{779,754}$  (which are novel or not commonly used in the literature) was highlighted. Such SVIs are worth more attention to ascertain their performance on other canopy types. Moreover, the hyperspectral analysis highlighted the suitability of the spectral regions related to water absorption features for LAI estimations [10,65].

The impact of grassland structural and biochemical heterogeneity on LAI estimations was demonstrated to be strong and, for this reason, no reliable field LAI estimation was possible at the spatial scale with any SVI. The results of the empirical approach were confirmed by the simulations performed with the RTM PROSAIL, when both structural and biochemical traits were co-varied. In this context, the uncertainties of satellite-based LAI products (in grassland canopies with either spatially or temporally-heterogeneous structure) need to be carefully taken into account adopting a modeling approach which is minimizing the impact of canopy structural heterogeneity. Despite the fact that the sensitivity analysis demonstrated that LAD impact is quite strong starting from 705 nm,  $RENDVI_{783,740}$  proved to be the best performing S-2-based SVIs for monitoring grasslands with heterogeneous structure. Given the fact that our study was carried out in two sites in the Alps, and that spatial observations were carried out only in a limited number of plots, more studies are needed in other grassland ecosystems and/or in other geographic areas to confirm the potential of SVIs using this spectral domain (alongside with the water absorption features) for vegetation monitoring, in the context of the Sentinel, GF-5 and PRISMA missions.

**Supplementary Materials:** The following are available online at <http://www.mdpi.com/2072-4292/12/14/2254/s1>, Figure S1: RGB images of the different plots at the IT-MBo study site used for spatial analysis. Figure S2: RGB images of the plot at the AT-Neu study site used for temporal analysis. Figure S3: The portable system used for spectral measurements at the IT-MBo for spatial scale observations. Table S1: Specifications of the multispectral instrument (MSI) and ocean and land color instrument (OLCI) on the S-2 and S-3 satellite system, respectively. The NIR-shoulder bands investigated in this study are shown in bold. Table S2: Summary of the statistics (N, Number of observations;  $R^2$ , Coefficient of determination; Adj.  $R^2$ , adjusted coefficient of determination; RMSE, Root mean square error) of the second-order polynomial regression between leaf area index (LAI,  $m^2 \cdot m^{-2}$ ) estimated from fraction of absorbed photosynthetically active radiation (fAPAR) and the spectral vegetation indices (SVIs) calculated from measured spectra for IT-MBo 2013, IT-MBo 2014 and AT-Neu 2018 at temporal scale observations and for IT-MBo 2017 at spatial scale observations. The three best-fitting models are highlighted in bold. Asterisk indicates significance of correlation: \*\*\*  $p < 0.001$ ; \*\*  $p < 0.01$ ; \*  $p < 0.05$ . n.s., not significant (Pearson's correlation test).

**Author Contributions:** Conceptualization, H.A.I., D.G., D.R., K.S., M.P.M. and L.V.; Data curation, H.A.I., K.S. and L.V.; Formal analysis, H.A.I., K.S. and L.V.; Methodology, H.A.I., D.G., D.R., M.D., K.S., M.P.M., G.W. and L.V.; Writing—original draft, H.A.I. and L.V.; and Review and editing, H.A.I., D.G., M.D., K.S., M.P.M., D.R., G.W. and L.V. All authors have read and agreed to the published version of the manuscript.

**Funding:** This project has received funding from the European Union’s Horizon 2020 research and innovation programme under the Marie Skłodowska-Curie grant agreement Nos. 721995 and 749323.

**Acknowledgments:** We want to thank the lab technicians Roberto Zampedri, Mauro Cavagna, Lorenzo Frizzera and Isaac Chini who supported in logistic operations and José Ramón Melendo-Vega who provided his guidance to understand the RTM and PROSAIL and helped to adopt the MATLAB code to run PROSAIL. This work was also supported by the FLUXPEC CGL2012-34383 and SynerTGE CGL2015-G9095-R (MINECO/FEDER, UE) projects.

**Conflicts of Interest:** The authors declare no conflict of interest.

## References

1. Martens, S.N.; Ustin, S.L.; Norman, J.M. Measurement of tree canopy architecture. *Int. J. Remote Sens.* **1991**, *12*, 1525–1545. [[CrossRef](#)]
2. Serrano, L.; Gamon, J.A.; Penuelas, J. Estimation of canopy photosynthetic and nonphotosynthetic components from spectral transmittance. *Ecology* **2000**, *81*, 3149–3162. [[CrossRef](#)]
3. Gianelle, D.; Vescovo, L. Determination of green herbage ratio in grasslands using spectral reflectance. Methods and ground measurements. *Int. J. Remote Sens.* **2007**, *28*, 931–942. [[CrossRef](#)]
4. Müller-Linow, M.; Pinto-Espinosa, F.; Scharr, H.; Rascher, U. The leaf angle distribution of natural plant populations: Assessing the canopy with a novel software tool. *Plant Methods* **2015**, *11*, 1–16. [[CrossRef](#)] [[PubMed](#)]
5. Ollinger, S.V. Sources of variability in canopy reflectance and the convergent properties of plants. *New Phytol.* **2011**, *189*, 375–394. [[CrossRef](#)]
6. Roelofsen, H.D.; van Bodegom, P.M.; Kooistra, L.; Witte, J.P.M. Predicting leaf traits of herbaceous species from their spectral characteristics. *Ecol. Evol.* **2014**, *4*, 706–719. [[CrossRef](#)]
7. Homolová, L.; Maalenovský, Z.; Shaepman, M.E.; García-Santos, G.; Clevers, J.G.P.W. Review of optical-based remote sensing for plant functional ecology. *Ecol. Complex.* **2013**, *15*, 1–16. [[CrossRef](#)]
8. Wang, R.; Gamon, J.A.; Cavender-Bares, J.; Townsend, P.A.; Zyguelbaum, A.I. The spatial sensitivity of the spectral diversity-biodiversity relationship: An experimental test in a prairie grassland. *Ecol. Appl.* **2018**, *28*, 541–556. [[CrossRef](#)] [[PubMed](#)]
9. Sakowska, K.; MacArthur, A.; Gianelle, D.; Dalponte, M.; Alberti, G.; Gioli, B.; Miglietta, F.; Pitacco, A.; Meggio, F.; Fava, F.; et al. Assessing Across-Scale Optical Diversity and Productivity Relationships in Grasslands of the Italian Alps. *Remote Sens.* **2019**, *11*, 614. [[CrossRef](#)]
10. Vescovo, L.; Gianelle, D. Using the MIR bands in vegetation indices for the estimation of grassland biophysical parameters from satellite remote sensing in the Alps region of Trentino (Italy). *Adv. Space Res.* **2008**, *41*, 1764–1772. [[CrossRef](#)]
11. Kumar, L.; Mutanga, O. Remote sensing of above-ground biomass. *Remote Sens.* **2017**, *9*, 935. [[CrossRef](#)]
12. Zarco-Tejada, P.J.; Hornero, A.; Hernández-Clemente, R.; Beck, P.S.A. Understanding the temporal dimension of the red-edge spectral region for forest decline detection using high-resolution hyperspectral and Sentinel-2a imagery. *ISPRS J. Photogramm. Remote Sens.* **2018**, *137*, 134–148. [[CrossRef](#)] [[PubMed](#)]
13. Kira, O.; Nguy-Robertson, A.L.; Arkebauer, T.J.; Linker, R.; Gitelson, A.A. Toward generic models for green LAI estimation in maize and soybean: Satellite observations. *Remote Sens.* **2017**, *9*, 318. [[CrossRef](#)]
14. Li, X.; Zhang, Y.; Bao, Y.; Luo, J.; Jin, X.; Xu, X.; Song, X.; Yang, G. Exploring the best hyperspectral features for LAI estimation using partial least squares regression. *Remote Sens.* **2014**, *6*, 6221–6241. [[CrossRef](#)]
15. Rouse, R.W.H.; Haas, J.A.W.; Deering, D.W. Monitoring Vegetation Systems in the Great Plains with ERTS. In Proceedings of the Third Earth Resources Technology Satellite-1 Symposium, Washington, DC, USA, 1 January 1974; pp. 309–317.
16. Fava, F.; Colombo, R.; Bocchi, S.; Meroni, M.; Sitzia, M.; Fois, N.; Zucca, C. Identification of hyperspectral vegetation indices for Mediterranean pasture characterization. *Int. J. Appl. Earth Obs. Geoinf.* **2009**, *11*, 233–243. [[CrossRef](#)]
17. Hansen, P.M.; Schjoerring, J.K. Reflectance measurement of canopy biomass and nitrogen status in wheat crops using normalized difference vegetation indices and partial least squares regression. *Remote Sens. Environ.* **2003**, *86*, 542–553. [[CrossRef](#)]

18. Nguy-Robertson, A.L.; Peng, Y.; Gitelson, A.A.; Arkebauer, T.J.; Pimstein, A.; Herrmann, I.; Karnieli, A.; Rundquist, D.C.; Bonfil, D.J. Estimating green LAI in four crops: Potential of determining optimal spectral bands for a universal algorithm. *Agric. For. Meteorol.* **2014**, *192–193*, 140–148. [[CrossRef](#)]
19. Delegido, J.; Verrelst, J.; Meza, C.M.; Rivera, J.P.; Alonso, L.; Moreno, J. A red-edge spectral index for remote sensing estimation of green LAI over agroecosystems. *Eur. J. Agron.* **2013**, *46*, 42–52. [[CrossRef](#)]
20. Xie, Q.; Dash, J.; Huang, W.; Peng, D.; Qin, Q.; Mortimer, H.; Casa, R.; Pignatti, S.; Laneve, G.; Pascucci, S.; et al. Vegetation Indices Combining the Red and Red-Edge Spectral Information for Leaf Area Index Retrieval. *IEEE J. Sel. Top. Appl. Earth Obs. Remote Sens.* **2018**, *11*, 1482–1492. [[CrossRef](#)]
21. Filella, I.; Peñuelas, J. The red edge position and shape as indicators of plant chlorophyll content, biomass and hydric status. *Int. J. Remote Sens.* **1994**, *15*, 1459–1470. [[CrossRef](#)]
22. Horler, D.N.H.; Dockray, M.; Barber, J. International Journal of Remote Sensing The red edge of plant leaf reflectance. *Remote Sens.* **1983**, *4*, 273–288. [[CrossRef](#)]
23. Frampton, W.J.; Dash, J.; Watmough, G.; Milton, E.J. Evaluating the capabilities of Sentinel-2 for quantitative estimation of biophysical variables in vegetation. *ISPRS J. Photogramm. Remote Sens.* **2013**, *82*, 83–92. [[CrossRef](#)]
24. Houborg, R.; Soegaard, H.; Boegh, E. Combining vegetation index and model inversion methods for the extraction of key vegetation biophysical parameters using Terra and Aqua MODIS reflectance data. *Remote Sens. Environ.* **2007**, *106*, 39–58. [[CrossRef](#)]
25. Atzberger, C.; Darvishzadeh, R.; Schlerf, M.; Le Maire, G. Suitability and adaptation of PROSAIL radiative transfer model for hyperspectral grassland studies. *Remote Sens. Lett.* **2013**, *4*, 55–64. [[CrossRef](#)]
26. Atzberger, C.; Darvishzadeh, R.; Immitzer, M.; Schlerf, M.; Skidmore, A.; le Maire, G. Comparative analysis of different retrieval methods for mapping grassland leaf area index using airborne imaging spectroscopy. *Int. J. Appl. Earth Obs. Geoinf.* **2015**, *43*, 19–31. [[CrossRef](#)]
27. Verrelst, J.; Malenovsky, Z.; Van der Tol, C.; Camps-Valls, G.; Gastellu-Etchegorry, J.P.; Lewis, P.; North, P.; Moreno, J. Quantifying Vegetation Biophysical Variables from Imaging Spectroscopy Data: A Review on Retrieval Methods. *Surv. Geophys.* **2019**, *40*, 589–629. [[CrossRef](#)]
28. Danner, M.; Berger, K.; Woche, M.; Mauser, W.; Hank, T. Fitted PROSAIL parameterization of leaf inclinations, water content and brown pigment content for winter wheat and maize canopies. *Remote Sens.* **2019**, *11*, 1150. [[CrossRef](#)]
29. Rossi, M.; Niedrist, G.; Asam, S.; Tonon, G.; Tomelleri, E.; Zebisch, M. A comparison of the signal from diverse optical sensors for monitoring alpine grassland dynamics. *Remote Sens.* **2019**, *11*, 296. [[CrossRef](#)]
30. Pettai, H.; Oja, V.; Freiberg, A.; Laisk, A. Photosynthetic activity of far-red light in green plants. *Biochim. Biophys. Acta Bioenerg.* **2005**, *1708*, 311–321. [[CrossRef](#)]
31. Zhen, S.; van Iersel, M.W. Photochemical Acclimation of Three Contrasting Species to Different Light Levels: Implications for Optimizing Supplemental Lighting. *J. Am. Soc. Hortic. Sci.* **2017**, *142*, 346–354. [[CrossRef](#)]
32. Gitelson, A.; Merzlyak, M.N. Spectral Reflectance Changes Associated with Autumn Senescence of *Aesculus hippocastanum* L. and *Acer platanoides* L. Leaves. Spectral Features and Relation to Chlorophyll Estimation. *J. Plant Physiol.* **1994**, *143*, 286–292. [[CrossRef](#)]
33. Gitelson, A.A.; Gritz, Y.; Merzlyak, M.N. Relationships between leaf chlorophyll content and spectral reflectance and algorithms for non-destructive chlorophyll assessment in higher plant leaves. *J. Plant Physiol.* **2003**, *160*, 271–282. [[CrossRef](#)]
34. Shang, J.; Liu, J.; Ma, B.; Zhao, T.; Jiao, X.; Geng, X.; Huffman, T.; Kovacs, J.M.; Walters, D. Mapping spatial variability of crop growth conditions using RapidEye data in Northern Ontario, Canada. *Remote Sens. Environ.* **2015**, *168*, 113–125. [[CrossRef](#)]
35. Sakowska, K.; Gianelle, D.; Zaldei, A.; Macarthur, A.; Carotenuto, F.; Miglietta, F.; Zampedri, R.; Cavagna, M.; Vesco, L. WhiteRef: A new tower-based hyperspectral system for continuous reflectance measurements. *Sensors* **2015**, *15*, 1088–1105. [[CrossRef](#)]
36. Vesco, L.; Wohlfahrt, G.; Balzarolo, M.; Pilloni, S.; Sottocornola, M.; Rodeghiero, M.; Gianelle, D. New spectral vegetation indices based on the near-infrared shoulder wavelengths for remote detection of grassland phytomass. *Int. J. Remote Sens.* **2012**, *33*, 2178–2195. [[CrossRef](#)]
37. Liu, L.Y.; Huang, W.J.; PU, R.L.; Wang, J.H. Detection of internal leaf structure deterioration using a new spectral ratio index in the near-infrared shoulder region. *J. Integr. Agric.* **2014**, *13*, 760–769. [[CrossRef](#)]

38. Delegido, J.; Verrelst, J.; Alonso, L.; Moreno, J. Evaluation of sentinel-2 red-edge bands for empirical estimation of green LAI and chlorophyll content. *Sensors* **2011**, *11*, 7063–7081. [[CrossRef](#)]
39. Cogato, A.; Pagay, V.; Marinello, F.; Meggio, F.; Grace, P.; Migliorati, M.D.A. Assessing the feasibility of using sentinel-2 imagery to quantify the impact of heatwaves on irrigated vineyards. *Remote Sens.* **2019**, *11*, 2869. [[CrossRef](#)]
40. Fernández-Manso, A.; Fernández-Manso, O.; Quintano, C. SENTINEL-2A red-edge spectral indices suitability for discriminating burn severity. *Int. J. Appl. Earth Obs. Geoinf.* **2016**, *50*, 170–175. [[CrossRef](#)]
41. Peng, Y.; Nguy-Robertson, A.; Arkebauer, T.; Gitelson, A.A. Assessment of canopy chlorophyll content retrieval in maize and soybean: Implications of hysteresis on the development of generic algorithms. *Remote Sens.* **2017**, *9*, 226. [[CrossRef](#)]
42. Curran, P.J.; Dungan, J.L.; Gholz, H.L. Exploring the relationship between reflectance red edge and chlorophyll content in slash pine. *Tree Physiol.* **1990**, *7*, 33–48. [[CrossRef](#)] [[PubMed](#)]
43. Jacquemoud, S.; Baret, F. PROSPECT: A model of leaf optical properties spectra. *Remote Sens. Environ.* **1990**, *34*, 75–91. [[CrossRef](#)]
44. Zarco-Tejada, P.J.; Miller, J.R.; Noland, T.L.; Mohammed, G.H.; Sampson, P.H. Scaling-Up and Model Inversion Methods with Narrowband Optical Indices for Chlorophyll Content Estimation in Closed Forest Canopies with Hyperspectral Data. *IEEE Trans. Geosci. Remote Sens.* **2001**, *39*, 1491–1507. [[CrossRef](#)]
45. Inoue, Y.; Guérif, M.; Baret, F.; Skidmore, A.; Gitelson, A.; Schlerf, M.; Darvishzadeh, R.; Oliso, A. Simple and robust methods for remote sensing of canopy chlorophyll content: A comparative analysis of hyperspectral data for different types of vegetation. *Plant Cell Environ.* **2016**, *39*, 2609–2623. [[CrossRef](#)]
46. Darvishzadeh, R.; Skidmore, A.; Schlerf, M.; Atzberger, C.; Corsi, F.; Cho, M. LAI and chlorophyll estimation for a heterogeneous grassland using hyperspectral measurements. *ISPRS J. Photogramm. Remote Sens.* **2008**, *63*, 409–426. [[CrossRef](#)]
47. Papale, D.; Migliavacca, M.; Cremonese, E.; Cescatti, A.; Alberti, G.; Balzarolo, M.; Beilelli Marchesini, L.; Canfora, E.; Casa, R.; Duce, P.; et al. Carbon, water and energy fluxes of terrestrial ecosystems in Italy. In *Environmental Science and Engineering*; Springer: Berlin/Heidelberg, Germany, 2014; Volume 131, pp. 11–45.
48. Wohlfahrt, G.; Hammerle, A.; Haslwanter, A.; Bahn, M.; Tappeiner, U.; Cernusca, A. Seasonal and inter-annual variability of the net ecosystem CO<sub>2</sub> exchange of a temperate mountain grassland: Effects of weather and management. *J. Geophys. Res. Atmos.* **2008**, *113*, 1–14. [[CrossRef](#)] [[PubMed](#)]
49. Wohlfahrt, G.; Sapinsky, S.; Tappeiner, U.; Cernusca, A. Estimation of plant area index of grasslands from measurements of canopy radiation profiles. *Agric. For. Meteorol.* **2001**, *109*, 1–12. [[CrossRef](#)]
50. Migliavacca, M.; Perez-Priego, O.; Rossini, M.; El-Madany, T.S.; Moreno, G.; van der Tol, C.; Rascher, U.; Berninger, A.; Bessenbacher, V.; Burkart, A.; et al. Plant functional traits and canopy structure control the relationship between photosynthetic CO<sub>2</sub> uptake and far-red sun-induced fluorescence in a Mediterranean grassland under different nutrient availability. *New Phytol.* **2017**, *214*, 1078–1091. [[CrossRef](#)]
51. Verrelst, J.; Rivera, J.P.; van der Tol, C.; Magnani, F.; Mohammed, G.; Moreno, J. Global sensitivity analysis of the SCOPE model: What drives simulated canopy-leaving sun-induced fluorescence? *Remote Sens. Environ.* **2015**, *166*, 8–21. [[CrossRef](#)]
52. Verrelst, J.; Rivera, J.P.; Veroustraete, F.; Muñoz-Marí, J.; Clevers, J.G.P.W.; Camps-Valls, G.; Moreno, J. Experimental Sentinel-2 LAI estimation using parametric, non-parametric and physical retrieval methods—A comparison. *ISPRS J. Photogramm. Remote Sens.* **2015**, *108*, 260–272. [[CrossRef](#)]
53. Sakowska, K.; Juszczak, R.; Gianelle, D. Remote Sensing of Grassland Biophysical Parameters in the Context of the Sentinel-2 Satellite Mission. *J. Sens.* **2016**, *2016*, 4612809. [[CrossRef](#)]
54. Verrelst, J.; Sabater, N.; Rivera, J.P.; Muñoz-Marí, J.; Vicent, J.; Camps-Valls, G.; Moreno, J. Emulation of leaf, canopy and atmosphere radiative transfer models for fast global sensitivity analysis. *Remote Sens.* **2016**, *8*, 673. [[CrossRef](#)]
55. Darvishzadeh, R.; Skidmore, A.; Schlerf, M.; Atzberger, C. Inversion of a radiative transfer model for estimating vegetation LAI and chlorophyll in a heterogeneous grassland. *Remote Sens. Environ.* **2008**, *112*, 2592–2604. [[CrossRef](#)]
56. Pasolli, L.; Asam, S.; Castelli, M.; Bruzzone, L.; Wohlfahrt, G.; Zebisch, M.; Notarnicola, C. Retrieval of Leaf Area Index in mountain grasslands in the Alps from MODIS satellite imagery. *Remote Sens. Environ.* **2015**, *165*, 159–174. [[CrossRef](#)]

57. Zhang, X.; Jiao, Z.; Dong, Y.; Zhang, H.; Li, Y.; He, D.; Ding, A.; Yin, S.; Cui, L.; Chang, Y. Potential investigation of linking PROSAIL with the Ross-Li BRDF model for vegetation characterization. *Remote Sens.* **2018**, *10*, 437. [[CrossRef](#)]
58. Melendo-Vega, J.R.; Martín, M.P.; Pacheco-Labrador, J.; González-Cascón, R.; Moreno, G.; Pérez, F.; Migliavacca, M.; García, M.; North, P.; Riaño, D. Improving the performance of 3-D radiative transfer model FLIGHT to simulate optical properties of a tree-grass ecosystem. *Remote Sens.* **2018**, *10*, 2061. [[CrossRef](#)]
59. Liu, Z.Z.; Li, W.; Yang, M. Two General Extension Algorithms of Latin Hypercube Sampling. *Math. Probl. Eng.* **2015**, *2015*, 450492. [[CrossRef](#)]
60. Prasad, B.; Carver, B.F.; Stone, M.L.; Babar, M.A.; Raun, W.R.; Klatt, A.R. Potential Use of Spectral Reflectance Indices as a Selection Tool for Grain Yield in Winter Wheat under Great Plains Conditions. *Crop Sci.* **2007**, *47*, 1426–1440. [[CrossRef](#)]
61. Babar, M.A.; Van Ginkel, M.; Klatt, A.R.; Prasad, B.; Reynolds, M.P. The potential of using spectral reflectance indices to estimate yield in wheat grown under reduced irrigation. *Euphytica* **2006**, *150*, 155–172. [[CrossRef](#)]
62. Gutierrez, M.; Reynolds, M.P.; Raun, W.R.; Stone, M.L.; Klatt, A.R. Spectral water indices for assessing yield in elite bread wheat genotypes under well-irrigated, water-stressed, and high-temperature conditions. *Crop Sci.* **2010**, *50*, 197–214. [[CrossRef](#)]
63. Peñuelas, J.; Gamon, J.A.; Fredeen, A.L.; Merino, J.; Field, C.B. Reflectance indices associated with physiological changes in nitrogen- and water-limited sunflower leaves. *Remote Sens. Environ.* **1994**, *48*, 135–146. [[CrossRef](#)]
64. Claudio, H.C.; Cheng, Y.; Fuentes, D.A.; Gamon, J.A.; Luo, H.; Oechel, W.; Qiu, H.-L.; Rahman, A.F.; Sims, D.A. Monitoring drought effects on vegetation water content and fluxes in chaparral with the 970 nm water band index. *Remote Sens. Environ.* **2006**, *103*, 304–311. [[CrossRef](#)]
65. Ustin, S.L.; Jacquemoud, S.; Pablo, J.Z.-T.; Asner, G.P. Remote Sensing of the Environment: State of the Science and New Directions. In *Remote Sensing for Natural Resources Management and Environment Monitoring*; Ustin, S.L., Ed.; Wiley: Hoboken, NJ, USA, 2004; pp. 679–729.
66. Sims, D.A.; Gamon, J.A. Estimation of vegetation water content and photosynthetic tissue area from spectral reflectance: A comparison of indices based on liquid water and chlorophyll absorption features. *Remote Sens. Environ.* **2003**, *84*, 526–537. [[CrossRef](#)]
67. Gitelson, A.; Garbuzov, G.; Szilagyi, F.; Mittenzwey, K.H.; Karnieli, A.; Kaiser, A. Quantitative remote sensing methods for real-time monitoring of inland waters quality. *Int. J. Remote Sens.* **1993**, *14*, 1269–1295. [[CrossRef](#)]
68. Dong, T.; Liu, J.; Shang, J.; Qian, B.; Ma, B.; Kovacs, J.M.; Walters, D.; Jiao, X.; Geng, X.; Shi, Y. Assessment of red-edge vegetation indices for crop leaf area index estimation. *Remote Sens. Environ.* **2019**, *222*, 133–143. [[CrossRef](#)]
69. Van der Tol, C.; Gonzalez-Cascon, R.; Moreno, G.; Carrara, A. senSCOPE: Modeling radiative transfer and biochemical processes in mixed canopies combining green and senescent leaves with SCOPE. *BioRxiv Ecol.* **2020**. [[CrossRef](#)]
70. Darvishzadeh, R.; Skidmore, A.; Atzberger, C.; van Wieren, S. Estimation of vegetation LAI from hyperspectral reflectance data: Effects of soil type and plant architecture. *Int. J. Appl. Earth Obs. Geoinf.* **2008**, *10*, 358–373. [[CrossRef](#)]
71. Zou, X.; Möttus, M. Sensitivity of common vegetation indices to the canopy structure of field crops. *Remote Sens.* **2017**, *9*, 994. [[CrossRef](#)]
72. Zhao, X.; Zhou, D.; Fang, J. Satellite-based Studies on Large-Scale Vegetation Changes in China. *J. Integr. Plant Biol.* **2012**, *54*, 713–728. [[CrossRef](#)]
73. Balzarolo, M.; Peñuelas, J.; Veroustraete, F. Influence of landscape heterogeneity and spatial resolution in multi-temporal in situ and MODIS NDVI data proxies for seasonal GPP dynamics. *Remote Sens.* **2019**, *11*, 1656. [[CrossRef](#)]
74. Aldakheel, Y.Y.; Danson, F.M. Spectral reflectance of dehydrating leaves: Measurements and modelling. *Int. J. Remote Sens.* **1997**, *18*, 3683–3690. [[CrossRef](#)]
75. Wen-long, B.; Qing-wei, Y.; Ya-jun, C.; Lu, Z.; Wei, L.; Hui-min, L.; Yong-qing, Y. Effects of Drought Stress on Photosynthetic Characteristics of Kentucky Bluegrass. *J. Northeast Agric. Univ. (Engl. Ed.)* **2013**, *20*, 19–23. [[CrossRef](#)]

76. Casas, A.; Riaño, D.; Ustin, S.L.; Dennison, P.; Salas, J. Estimation of water-related biochemical and biophysical vegetation properties using multitemporal airborne hyperspectral data and its comparison to MODIS spectral response. *Remote Sens. Environ.* **2014**, *148*, 28–41. [[CrossRef](#)]
77. Miraglio, T.; Adeline, K.; Huesca, M.; Ustin, S.; Briottet, X. Monitoring LAI, Chlorophylls, and Carotenoids Content of a Woodland Savanna Using Hyperspectral Imagery and 3D Radiative Transfer Modeling. *Remote Sens.* **2019**, *12*, 28. [[CrossRef](#)]
78. Gitelson, A.A.; Chivkunova, O.B.; Merzlyak, M.N. Nondestructive estimation of anthocyanins and chlorophylls in anthocyanic leaves. *Am. J. Bot.* **2009**, *96*, 1861–1868. [[CrossRef](#)] [[PubMed](#)]



© 2020 by the authors. Licensee MDPI, Basel, Switzerland. This article is an open access article distributed under the terms and conditions of the Creative Commons Attribution (CC BY) license (<http://creativecommons.org/licenses/by/4.0/>).